

## Satellite and CALJET Aircraft Observations of Atmospheric Rivers over the Eastern North Pacific Ocean during the Winter of 1997/98

F. MARTIN RALPH, PAUL J. NEIMAN, AND GARY A. WICK

*NOAA/Environmental Technology Laboratory, Boulder, Colorado*

(Manuscript received 20 November 2003, in final form 16 January 2004)

### ABSTRACT

This study uses a unique combination of airborne and satellite observations to characterize narrow regions of strong horizontal water vapor flux associated with polar cold fronts that occurred over the eastern North Pacific Ocean during the winter of 1997/98. Observations of these “atmospheric rivers” are compared with past numerical modeling studies to confirm that such narrow features account for most of the instantaneous meridional water vapor transport at midlatitudes.

Wind and water vapor profiles observed by dropsondes deployed on 25–26 January 1998 during the California Land-falling Jets Experiment (CALJET) were used to document the structure of a modest frontal system. The horizontal water vapor flux was focused at low altitudes in a narrow region ahead of the cold front where the combination of strong winds and large water vapor content were found as part of a low-level jet. A close correlation was found between these fluxes and the integrated water vapor (IWV) content. In this case, 75% of the observed flux through a 1000-km cross-front baseline was within a 565-km-wide zone roughly 4 km deep. This zone contained  $1.5 \times 10^8 \text{ kg s}^{-1}$  of meridional water vapor flux, the equivalent of  $\sim 20\%$  of the global average at  $35^\circ\text{N}$ .

By compositing polar-orbiting satellite Special Sensor Microwave Imager (SSM/I) data from 46 dates containing long, narrow zones of large IWV, it was determined that the single detailed case was representative of the composite in terms of both the IWV amplitude (3.09 cm vs 2.81 cm) and the width of the area where  $\text{IWV} \geq 2 \text{ cm}$  (424 km vs 388 km). The SSM/I composites also showed that the width scales (defined by the 75% cumulative fraction along a 1500-km cross-plume baseline) for cloud liquid water and rain rate were 176 and 141 km, respectively, which are narrower than the 417 km for IWV. Examination of coincident Geostationary Operational Environmental Satellite (GOES) and SSM/I satellite data revealed that GOES cloud-top temperatures were coldest and cloud-top pressures were lowest in the core of the IWV plumes, and that the core cloud tops became substantially colder and deeper for larger IWV. A strong latitudinal dependence of the satellite-derived cross-river characteristics was also found.

Atmospheric rivers form a critical link between weather and climate scales. They strongly influence both short-term weather and flood prediction, as well as seasonal climate anomalies and the global water cycle, through their cumulative effects. However, the rivers remain poorly observed by the existing global atmospheric observing system in terms of their horizontal water vapor fluxes.

### 1. Introduction

The distribution and transport of water vapor in the atmosphere is critical to a range of issues extending from the issuance of flood warnings to initialization of numerical weather prediction models and to understanding the hydrological and global climate systems. From both weather and climate perspectives it is well known that a key contributor to the advection of water vapor is the low-level jet (LLJ), which is found in the warm sectors of extratropical cyclones (e.g., Namias 1939; Bonner 1968; Palmén and Newton 1969; Browning and Pardoe 1973; Cotton and Anthes 1989; Bluestein 1993) and as

part of diurnal oscillations over the Great Plains (e.g., Bonner 1968; Stensrud 1996; Whiteman et al. 1997). The type of LLJ that is the focus of this paper is part of a broader region of generally poleward heat transport within extratropical cyclones that is referred to as the “warm conveyor belt” (e.g., Browning 1990; Carlson 1991). The warm conveyor belt is an integral component of extratropical cyclones that plays a key role in transporting sensible and latent heat poleward, balancing the equatorward transport of relatively cool, dry air in other branches of the extratropical cyclone’s circulation.

This paper focuses on a subset of the total heat transport, that is, the poleward meridional water vapor flux. For a variety of reasons its distribution can evolve differently from that of the sensible heat flux component, for example, the sources and sinks of water vapor differ markedly from those of sensible heat. Recently, in a

---

*Corresponding author address:* Dr. F. Martin Ralph, NOAA/Environmental Technology Laboratory, Mail Code R/ET7, 325 Broadway, Boulder, CO 80305.  
E-mail: MartyRalph@noaa.gov

numerical modeling study using European Centre for Medium-Range Weather Forecasts global analyses, Zhu and Newell (1998) explored the role of extratropical cyclones in meridional water vapor transport. By establishing a threshold value of meridional water vapor flux they segregated daily fluxes at each grid point as either “broad” fluxes or “river” fluxes. Based on this segregation, it was possible to determine how much of the total meridional flux at a given latitude was attributable to atmospheric rivers and to diagnose the meridional width scale of these features at a given latitude, at least from the model perspective. They concluded that >90% of the total meridional water vapor flux in the midlatitudes was accomplished by “atmospheric rivers” covering <10% of the total hemispheric circumference. The term “atmospheric river”<sup>1</sup> appropriately emphasizes both their filamentary nature and the focus on water vapor. This also suitably distinguishes it from the broader region characterized as the warm conveyor belt with its mixture of both sensible and latent heat components.

Zhu and Newell (1998) also found that four to five such rivers are usually present at any given time. This corresponds well to planetary wavenumber 4–5, which is often found during Northern Hemisphere cool seasons. This correspondence likely results from the fact that each planetary wave normally has associated with it a synoptic-scale extratropical cyclone, which in turn usually has large- and mesoscale frontal processes that can give rise to a narrow region of strong meridional water vapor flux. However, the position of the planetary waves relative to the continents, major land surface features, and oceans can also strongly influence their impact on global meridional water vapor transport. For example, an extratropical cyclone entraining dry air from a continental region will not be effective at transporting large amounts of water vapor until it taps into an area with greater moisture content. This is often seen when extratropical cyclones move from North America’s Rocky Mountains onto the Great Plains where they can then entrain water vapor from the Gulf of Mexico (e.g., Palmén and Newton 1969). Although this paper does not address these issues of ocean versus land or of the planetary wave pattern, it does inform future research on these topics.

It should be noted that a set of earlier studies focused on middle- and upper-tropospheric cloud bands (and their implied regions of enhanced water vapor transport) using primarily infrared satellite images. Thepenier and Cruette (1981) documented the evolution of distinctive, long bands of mid- and high clouds that could stretch

thousands of kilometers. This study was extended using more cases to document the origins of these cloud bands that mark a linkage between the Tropics and the extratropics (McGuirk et al. 1987; Kuhnel 1989; Iskenderian 1995). While these studies revealed important aspects of the cloud bands, including the role of tropical and extratropical triggers, they were unable to document the actual water vapor content within the bands (including conditions at lower altitudes where the most water vapor exists), which is the focus of the study presented here.

The role of the LLJ (and of atmospheric rivers) in producing heavy rainfall has been explored in complex terrain where orographic lifting of the moist, and often potentially unstable, air mass can create heavy rainfall (Reynolds and Kuciauskas 1988; Heggli and Rauber 1988; Neiman et al. 2002; Ralph et al. 2003). This relationship, along with limitations in observations of the LLJ offshore and along the U.S. West Coast, motivated the California Land-falling Jets Experiment (CALJET) that was conducted along and offshore of the California coast in the winter of 1997/98 (Ralph et al. 1999). The CALJET campaign, led by the National Oceanic and Atmospheric Administration’s (NOAA) Environmental Technology Laboratory (ETL), resulted in improved understanding of the role of the LLJ in modulating orographic rainfall (Neiman et al. 2002) and flooding (Ralph et al. 2003) and produced a dataset designed to explore the connections between short-term climate variability and extreme weather events in a record wet winter. Atmospheric rivers form such a linkage and will be the focus of the observational study presented here. A primary goal of this study is the use of observations to evaluate the model-based conclusions of Zhu and Newell (1998), which used a model with effective grid size of 200 km that may not have adequately resolved the rivers. Specific questions addressed in our paper include, what is the magnitude of the horizontal water vapor flux in a well-observed moderate-intensity oceanic storm, and what are its characteristic width and depth scales? How do the case study results compare with composites derived from satellite data? What are the capabilities and limitations of existing satellite-observing systems with respect to detecting key aspects of atmospheric rivers over oceans for forecasting and climate monitoring?

The paper first describes the key ground-based, airborne, and satellite-observing systems deployed by or utilized by CALJET. The synoptic and mesoscale characteristics of a well-observed atmospheric river over the eastern Pacific are summarized, resulting in a detailed snapshot of an atmospheric river from dropsonde data. The representativeness of this case study is then examined using satellite data from the entire winter season of 1997/98, which also are used to diagnose key characteristics of the distributions of integrated water vapor, cloud liquid water, rain rate, ocean-surface wind speed, cloud-top temperature, and cloud-top pressure.

---

<sup>1</sup> This term, or its related version “tropospheric rivers” was introduced by Newell et al. (1992) and has been used since then by Zhu and Newell (1994) in a study relating them to rapid extratropical cyclogenesis, by Smirnov and Moore (1999, 2001) in studies of water vapor transport into the McKenzie River basin of northwestern Canada, and by Zhu et al. (2000) in a study of upper-tropospheric water vapor transport.

## 2. Observing platforms

A suite of research observing platforms was deployed for CALJET across coastal California and the data-sparse eastern Pacific (Ralph et al. 1999), complementing the established operational observing systems. A NOAA P-3 turboprop research aircraft measured standard meteorological parameters every 1 s during a flight at its highest operating altitude (500–400 mb) and released 29 Global Positioning System (GPS) dropsondes through a polar frontal zone offshore of California between 2003 UTC 25 January and 0447 UTC 26 January 1998. The dropsondes provided high-resolution vertical profiles of wind velocity, temperature, and water vapor. A lower-fuselage scanning C-band ( $\sim 5.6$  cm wavelength) radar provided reflectivity measurements of precipitation elements.

Research data collected from three 915-MHz wind profilers (e.g., Ecklund et al. 1988; Carter et al. 1995) operated by NOAA/ETL were utilized in this study. These profilers, located at Bodega Bay (BBY), Point Arena (PAA), and Eureka (ERK), provided hourly averaged vertical profiles of horizontal wind velocity from  $\sim 0.1$  to 4.0 km above ground level (AGL) with  $\leq 100$  m vertical resolution in clear, cloudy, and precipitating conditions. The profiler winds were objectively edited using the vertical–temporal continuity method of Weber et al. (1993). The height of the precipitation melting level was determined objectively using the brightband detection method of White et al. (2002). At each profiler site a tipping-bucket rain gauge measured rainfall with 0.01-in. ( $\sim 0.25$  mm) resolution, while observations of wind, temperature, moisture, and pressure were collected from a 10-m tower, all with 2-min sampling.

Operational polar-orbiting and Geostationary Operational Environmental Satellites (GOES) also furnished observations. A Special Sensor Microwave Imager (SSM/I) was carried on three Defense Meteorological Satellite Program polar orbiters (*F11*, *F13*, *F14*) that circled the globe once every  $\sim 102$  min. Tropospheric integrated water vapor (IWV) (Schuessel and Emery 1990), cloud liquid water (CLW) (Weng and Grody 1994), rain rate (RR) (Ferriday and Avery 1994), and ocean-surface wind speed (SPD) (Goodberlet et al. 1990) were retrieved from each SSM/I sensor over a 1400-km-wide swath and gridded at 25-km resolution. The SSM/I measurements are remarkably reliable (Wentz 1997), although two important exceptions should be noted: 1) IWV measurements can be degraded in heavy rain, and 2) useful retrievals of surface wind speed are not possible at all when rain is present. The SSM/I sampling is synoptic and somewhat irregular in timing and location, and retrievals are generally not available over land. A pair of GOES satellites (*GOES-8/9*) provided nearly continuous spatiotemporal observations over the Pacific and adjacent landmasses with their infrared, visible, and upper-tropospheric water vapor sensors, and they also yielded 3-hourly measure-

ments of tropospheric feature-tracked winds when combined with operational numerical model forecasts (Velden et al. 1997; Nieman et al. 1997). The infrared sensors, in combination with operational model output, provided measurements of cloud-top temperature (CTT) and cloud-top pressure (CTP). A sounder package on each GOES satellite furnished radiance observations that were ingested into a nonlinear physical retrieval algorithm to generate IWV retrievals (Rao and Fuelberg 1998; Menzel et al. 1998; Ma et al. 1999). Unlike the polar-orbiting microwave sensors, the GOES sensors provide excellent areal and temporal IWV coverage; that is, the same geographical area is scanned each hour and coverage includes both ocean and land, and the effective resolution is  $\sim 14$  km. However, also unlike the microwave data, clouds contaminate the GOES retrievals (e.g., Lipton 1998), which is disadvantageous over the moisture-laden Pacific. In addition, the GOES retrievals depend on numerical models for a first guess.

Ground-based operational observing systems were also used in this study. California's Automated Local Evaluation in Real Time (ALERT; Mendell 1992) network of  $\sim 900$  rain gauges measured rainfall with 0.04-in. ( $\sim 1.0$  mm) resolution as frequently as every 15 min. The rain gauge data were quality controlled, including identification of sites where missing data would have biased storm-total precipitation analyses. Hourly surface meteorological observations were obtained from airports and moored and drifting buoys, while 3-h meteorological data were acquired from ocean-borne ships. Rawinsondes from Oakland (OAK) provided 12-h thermodynamic and wind soundings.

## 3. A case study of a polar frontal zone

This section utilizes the 29 GPS dropsondes deployed on 25–26 January 1998 to document the mesoscale spatial distribution of water vapor, and its horizontal transport, through a modest polar frontal zone over the eastern Pacific. These dropsondes afforded a uniquely well-resolved ( $\sim 100$  km resolution) picture of the system as it approached the California coast. The dropsonde-based mesoscale discussion is preceded by a brief description of the synoptic-scale conditions.

### a. Synoptic overview

The event studied here was associated with a polar cold-frontal zone that was laid out over the eastern Pacific by a major synoptic-scale cyclone with a central pressure of  $\sim 962$  mb near  $48^\circ\text{N}$  and  $135^\circ\text{W}$  at 0000 UTC 26 January 1998 (Fig. 1a). The storm's cloud field possessed a wrapped-up comma-cloud head spiraling outward from the cyclone center and a comma-cloud tail extending offshore of California with the trailing cold front (Fig. 1b). The P-3 flight track and locations of the 29 dropsondes are shown in Fig. 2, where it is evident that the aircraft transected the cold-frontal cloud

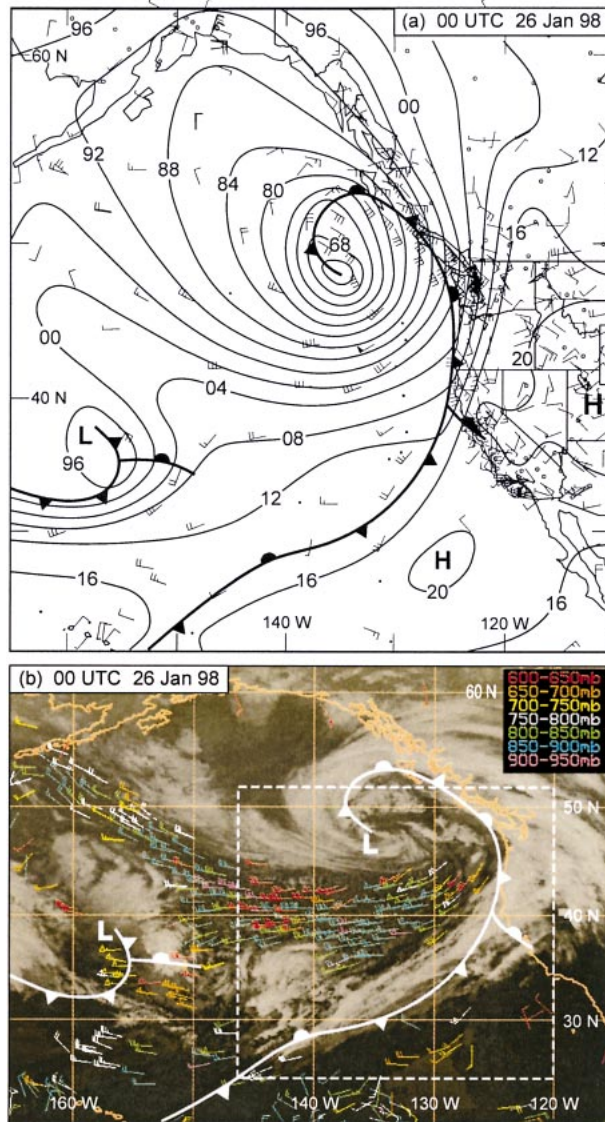


FIG. 1. (a) Sea level pressure (SLP) analysis at 0000 UTC 26 Jan 1998. Wind flags =  $25 \text{ m s}^{-1}$ , full bars =  $5 \text{ m s}^{-1}$ , and half bars =  $2.5 \text{ m s}^{-1}$ . Stand-alone solid dots represent surface observations of SLP with missing winds. The ocean-based observations are from 3-h ship and 1-h buoy reports. Standard frontal notation is used. (b) NOAA GOES infrared satellite image and satellite-derived winds below 600 mb (color coded for altitude) at 0000 UTC 26 Jan 1998. Winds and fronts are as in (a). The dashed inset box defines the domain for Fig. 2.

band three times within the inset mesoscale domain. This track was time-to-space adjusted to 0000 UTC 26 January 1998 using a phase speed of the overall frontal system ( $7.3 \pm 2.0 \text{ m s}^{-1}$  from  $332^\circ$ ) derived from sequential satellite images. This slow phase speed meant that individual dropsonde positions at the beginning and end of the flight were adjusted at most by 110 km.

The cold front produced significant rainfall in northern California, with up to 110 mm in 36 h along a 150-km stretch of coast (Fig. 3). The sharp along-coast gra-

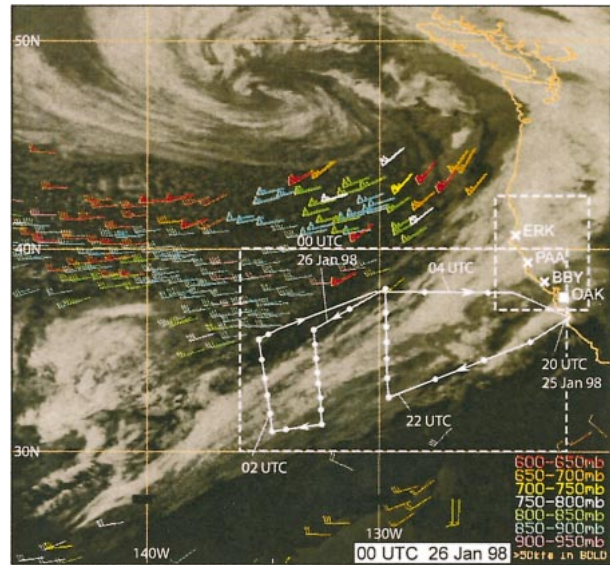


FIG. 2. Same satellite image as in Fig. 1b, except zoomed in. The P-3 flight track (white) is time-to-space adjusted to 0000 UTC 26 Jan 1998 using a phase velocity of  $7.3 \text{ m s}^{-1}$  from  $332^\circ$ . The locations of the 29 dropsondes along the flight track are portrayed with bold white dots. Key wind profiler sites are marked with an "x" and labeled with their three-letter names, and the Oakland rawinsonde site is labeled "OAK." The large dashed inset box defines the domain for Figs. 5–7, and the small dashed inset box corresponds to the domain in Fig. 3.

dient north and south of this region resulted partially from the slow-moving nature of the frontal system responsible for much of the rain and reflects the importance of a narrow, but intense, plume of moisture found offshore (see sections 3b and 3c). The steady character of the prefrontal southerly component wind flow, the brightband height, and the rain rate was captured by the PAA wind profiler within the core of the heavy coastal rainfall (Fig. 4). Much less rain fell at the adjacent wind-profiler sites at BBY and ERK. Rainfall at PAA ceased following the cold-frontal passage between 2200 UTC 25 January and 0000 UTC 26 January and the onset of postfrontal westerlies.

### b. Mesoscale plan-view perspective

Mesoscale plan-view analyses were constructed from the dropsondes in the inset domain of Fig. 2. A subjective potential temperature ( $\theta$ ) analysis at 1000 mb (Fig. 5) reveals two frontal zones rather than the single zone depicted in the synoptic analysis (Fig. 1a). The single zone in Fig. 1a is the leading—that is, the southeasternmost—of the multiple cold frontal zones shown in the mesoscale analyses. Each front exhibited a wind direction shift and a  $\sim 2 \text{ K}$  decrease in  $\theta$ . The southern front also corresponded with a rope cloud noted in visible satellite imagery (not shown), which helped anchor the analyzed near-surface position of this front. The availability of three cross-front dropsonde legs estab-

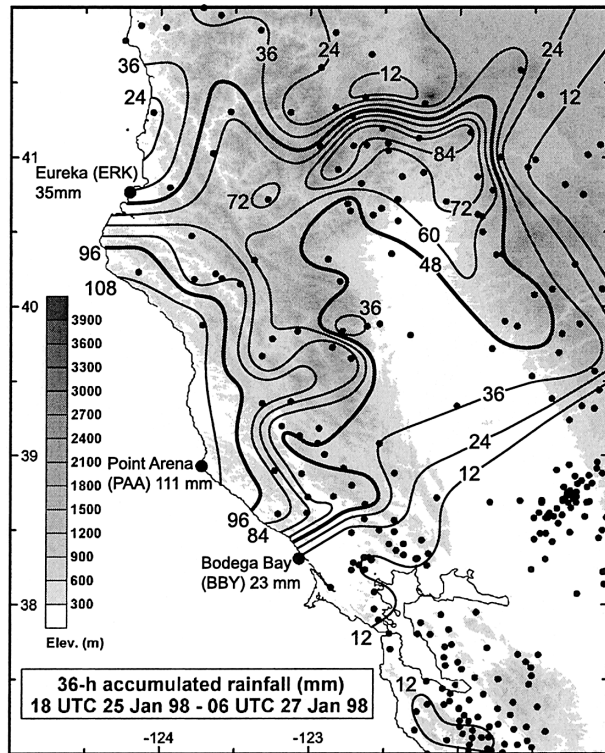


FIG. 3. Terrain base map with a 36-h accumulated rainfall analysis (mm) between 1800 UTC 25 Jan and 0600 UTC 27 Jan 1998. The small dots show the ALERT rain gauge sites used for the analysis, and the three large dots mark the wind-profiler sites shown in Fig. 2; the 36-h accumulated rainfall at these three sites are listed.

lished that the fronts were nearly parallel to each other and were separated by ~250 km. The northern front created its own narrow, but well-defined, warm tongue, leaving a narrow zone of cooler air between the fronts. Other case studies with offshore aircraft data from the Coastal Observation and Simulation with Topography (COAST; Chien et al. 2001) and CALJET (Ralph et al. 2003; Neiman et al. 2004) field studies in the region have shown that surface polar cold fronts have appeared as multiple transitions in other events as well. However, the reasons for this behavior are not yet well understood.

A mesoscale depiction of the horizontal IWV distribution across the fronts is shown in Fig. 6. An axis of large IWV was cradled between the 1000-mb fronts, illustrating the elongated and narrow nature of the IWV plume. Values of IWV exceeding 2 cm were confined to a region only 424 km wide, and values >3 cm spanned only 70 km in the cross-front direction. Because the P-3 flew slightly above 500 mb, the dropsonde-based IWV values include the contribution of water vapor only below 500 mb. Based on the December–January–February mean vertical profile of water vapor specific humidity for the Northern Hemisphere by Peixoto and Oort (1992), the layer below 500 mb contributes ~98% to the IWV on this seasonal hemispheric average. Similarly, rawinsonde launches from Oakland within the

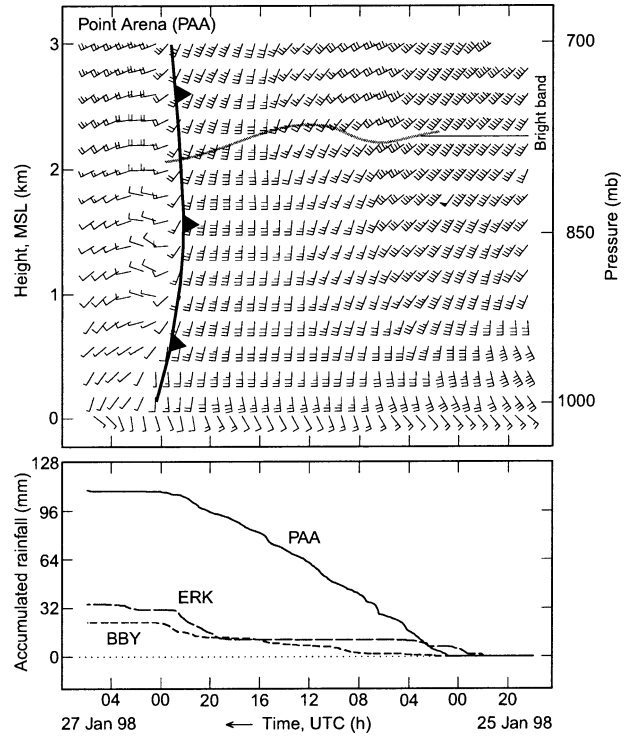


FIG. 4. Wind-profiler and rainfall data between 1800 UTC 25 Jan and 0600 UTC 27 Jan 1998: (top) Time–height section of hourly wind profiles (flags and barbs are as in Fig. 1) and brightband height (gray-shaded line) measured by the PAA wind profiler. Standard frontal notation is used. (bottom) Time series of accumulated rainfall at the three wind-profiler sites (e.g., PAA, BBY, and ERK).

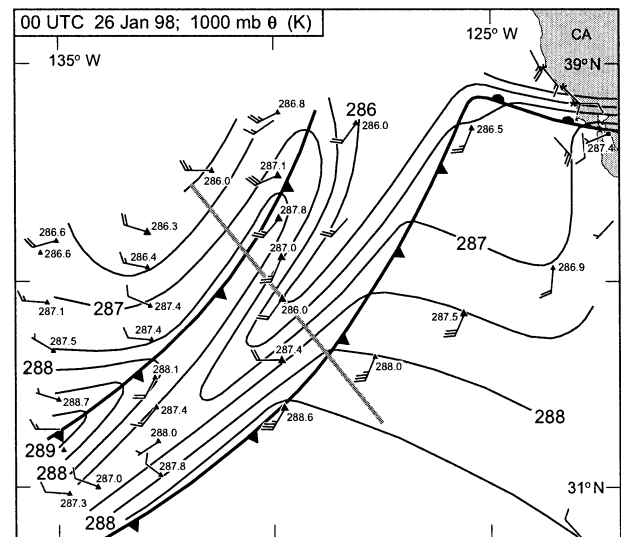


FIG. 5. The 1000-mb potential temperature ( $\theta$ , K) and frontal analysis at 0000 UTC 26 Jan 1998, based on the P-3 dropsondes (triangle vector heads) and the Oakland rawinsonde (square head); the numerical values of  $\theta$  are plotted. Surface winds from nearby wind profilers (star heads; labeled in Fig. 3), and ships and buoys (no heads) are also shown. Wind flags and barbs are as in Fig. 1. The bold gray-shaded line is a projection line for the cross section in Fig. 8; the eight dropsondes included in this cross section are marked with large triangle vector heads.

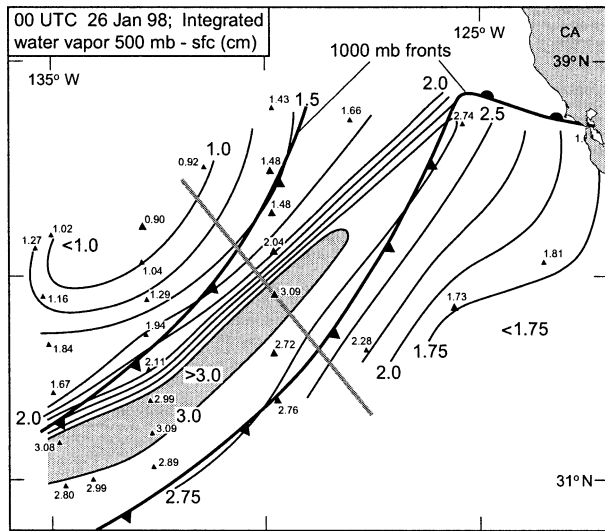


FIG. 6. Vertically integrated water vapor (cm) analysis from the surface to 500 mb at 0000 UTC 26 Jan 1998, based on the dropsondes (triangles) and Oakland rawinsonde; the numerical values of IWV are plotted. The fronts, bold gray-shaded line, and large triangles are as in Fig. 5.

moisture plume at 1200 UTC 26 January and 0000 UTC 27 January documented a mean IWV of 2.64 cm, 96.3% of which was contained below 500 mb. Hence, the dropsonde IWV values are representative of the full-tropospheric values to within <math><5\%</math>.

The water vapor specific humidity fields at 1000 and 700 mb (Figs. 7a and 7b) reveal very different distributions of moisture in the lower and middle troposphere. At 1000 mb, the greatest moisture content (>math>10\text{ g kg}^{-1}</math>) was ahead of the leading cold front, and a modest decrease of

sharper moisture gradient resided behind the trailing cold front. In contrast, a plume of high moisture content at 700 mb (>math>5\text{ g kg}^{-1}</math>) was positioned between the 1000-mb fronts, with lesser values on the warm side of the leading front. The moisture gradient on the poleward or cold side of the moisture plume at 700 mb was much tighter than its counterpart at 1000 mb. The 700-mb specific humidity field (Fig. 7b) bears striking resemblance to the IWV analysis (Fig. 6), whereas the 1000-mb field (Fig. 7a) is decidedly different. The following subsection provides a meteorological explanation for the vertical variation in horizontal moisture distribution.

c. Anatomy of an atmospheric river

The vertical structure of the specific humidity (\sim 850 mb, where it became horizontal. Farther north, this zone extended up to 600 mb, where a distinct region of midtropospheric drying was present north of a narrow but deep wedge of moisture situated at the northern end of a larger-scale plume of enhanced prefrontal moisture. Flight-level observations and airborne radar data from the P-3 reveal that deep convection was triggered in a line within this narrow wedge, where a convective updraft and maximum cloud liquid water was also observed (see Fig. 8a). Sub-

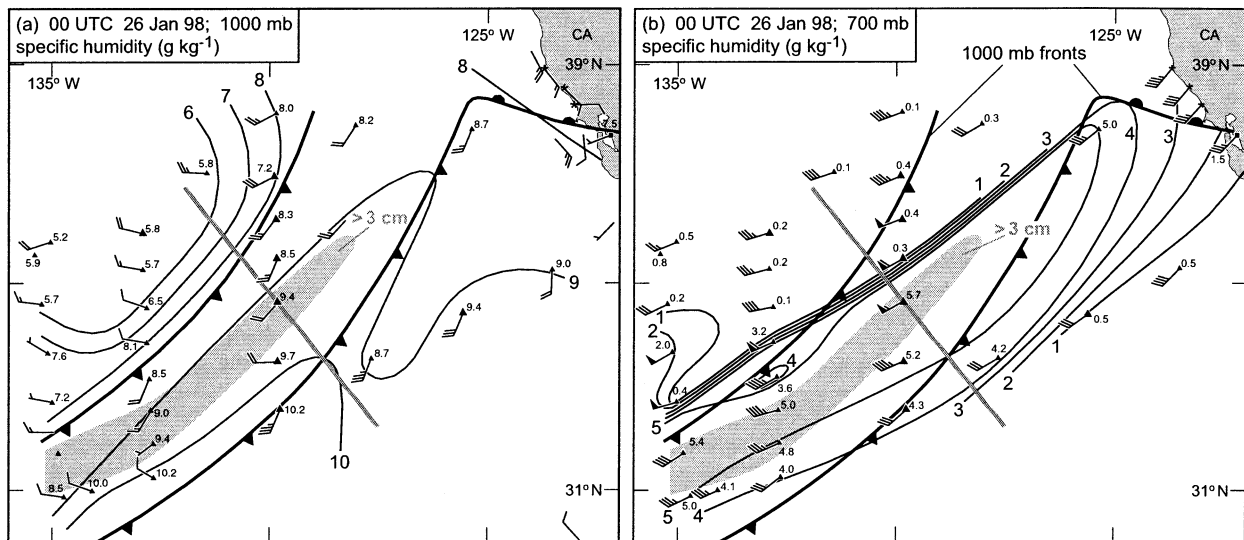


FIG. 7. Water vapor specific humidity analysis (

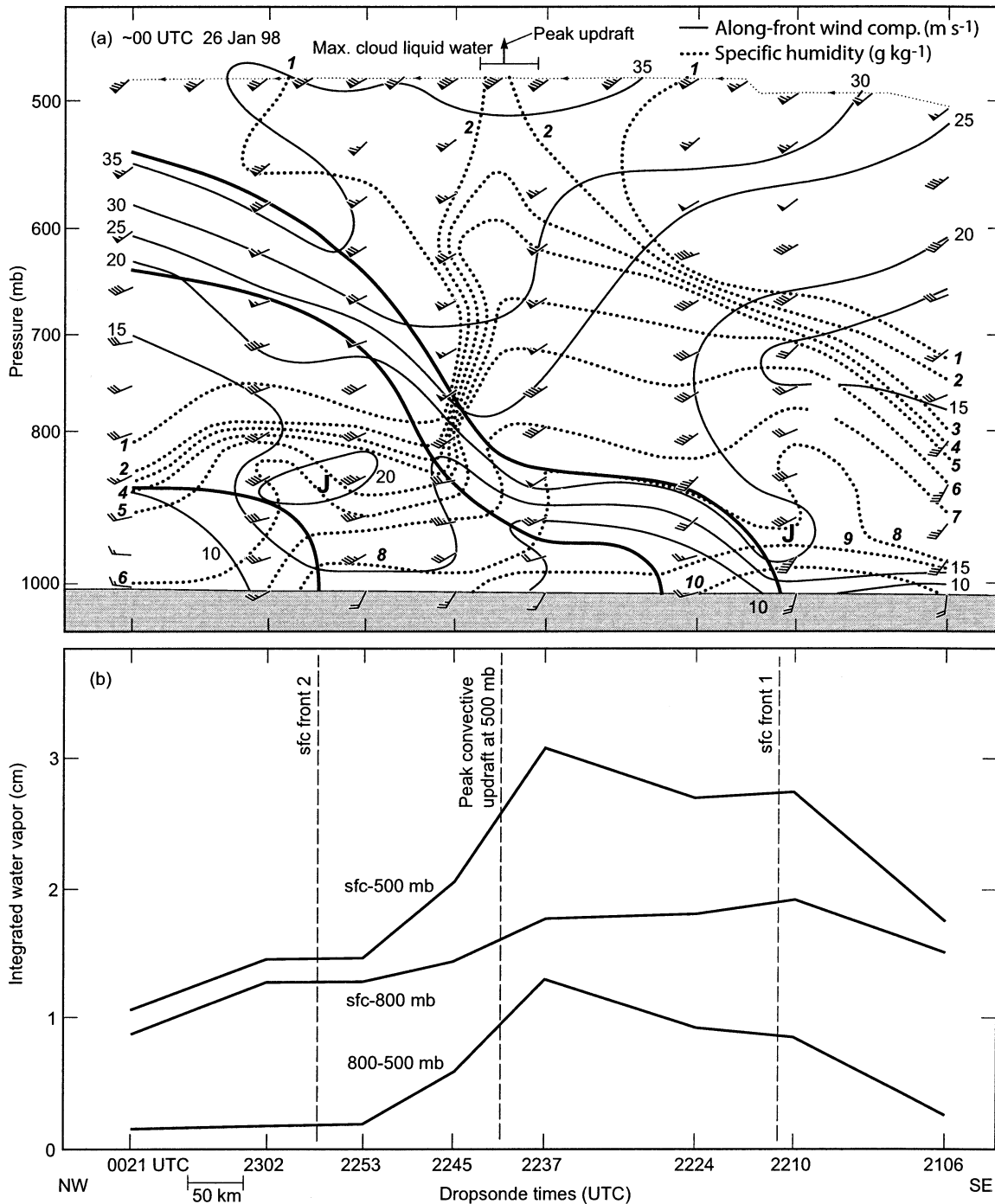


FIG. 8. (a) Cross section of alongfront wind speed (solid contours,  $m s^{-1}$ ; directed from  $225^\circ$ ) and specific humidity (dotted contours,  $g kg^{-1}$ ) along the gray-shaded projection line in Figs. 5–7. Frontal boundaries are marked with bold black lines. Wind flags and bars are as in Fig. 1. The flight track is portrayed with a thin dotted line near 500 mb, and the maximum cloud liquid water (bracket) and peak convective updraft (arrow) along this flight leg are labeled. (b) Traces of IWV (cm) from the dropsondes for three layers (surface–500 mb, surface–800 mb, and 800–500 mb). The times (UTC) of dropsonde deployments on 25 and 26 Jan 1998 are given.

sidence behind this deep convection is likely responsible for the drying ahead of the front above  $\sim 800$  mb through the downward advection of drier air from higher elevations. An axis of maximum  $U$  coincided with the

warm side of the front, with evidence of an LLJ at 900 mb in the vicinity of a second, shallower wedge of moisture at the southern end of the larger-scale plume. The northern front was quite shallow but, as with its southern

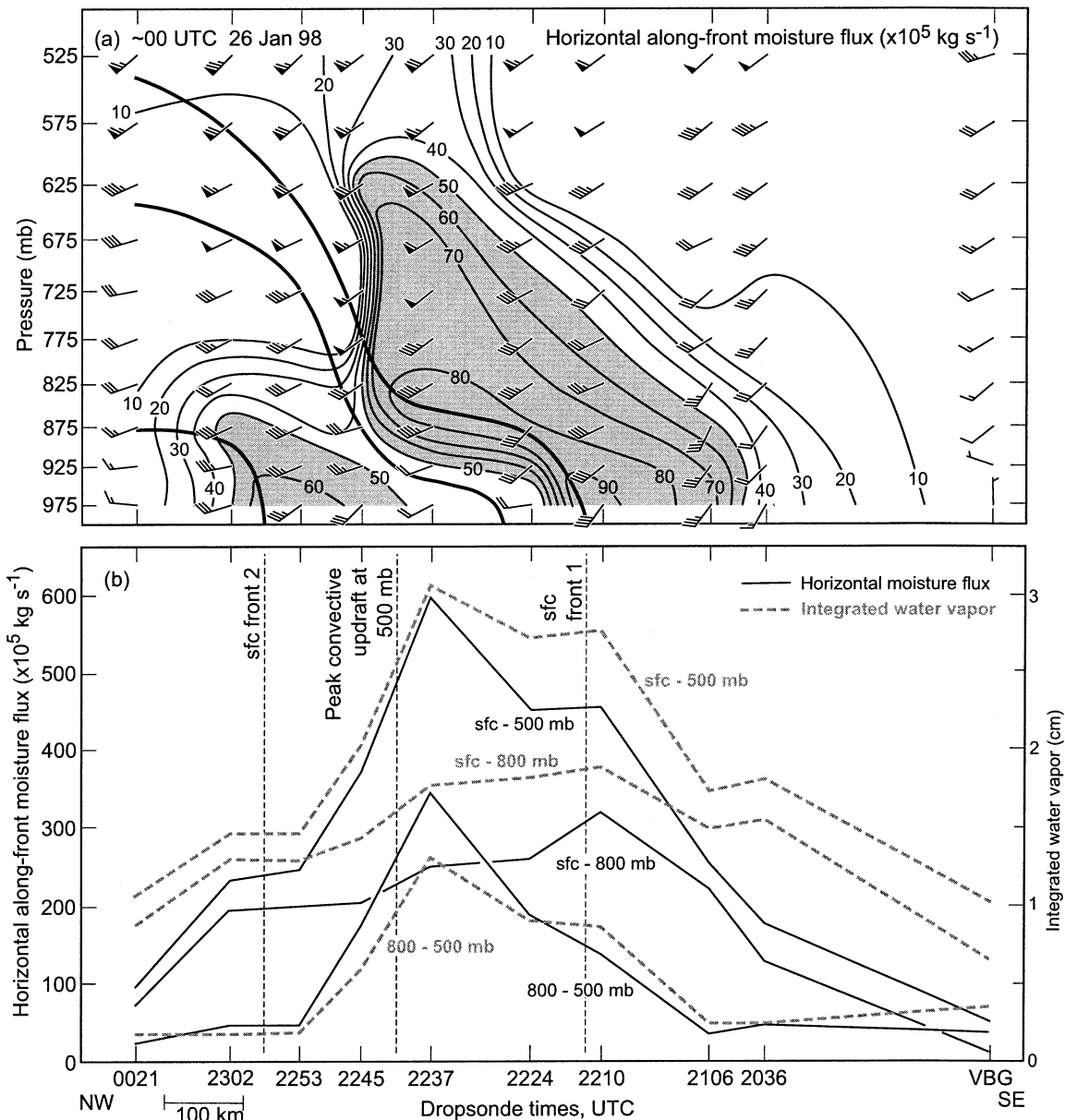


FIG. 9. (a) Cross section of horizontal alongfront moisture flux  $F_h$  ( $\times 10^5 \text{ kg s}^{-1}$ ; directed from  $225^\circ$ ) along the gray-shaded projection line in Figs. 5–7. Fronts are as in Fig. 8. This section extends southeastward beyond the projection line, because an additional dropsonde at 2036 UTC 25 Jan and the rawinsonde at VBG at 0000 UTC 26 Jan 1998 were included in the analysis; 50-mb-averaged wind velocities are shown (flags and barbs are as in Fig. 1). (b) Traces of  $F_h$  (solid black;  $\times 10^5 \text{ kg s}^{-1}$ ) and IWV (gray-shade dashed; cm) from the soundings for three layers (surface–500 mb, surface–800 mb, and 800–500 mb). The times (UTC) of dropsonde deployments on 25 and 26 Jan 1998 are given.

partner, it too possessed a prefrontal LLJ and water vapor plume. The key features of this cross section were also found in data from the two other cross-front dropsonde legs (not shown), thus adding confidence to the analyzed vertical structure.

Figure 8b reveals the IWV distribution along the cross section. Although there is a significant northward increase in the surface–500-mb IWV toward the southern surface front, the largest value, 3.09 cm, reflects the

deep moisture in the vicinity of the convection ahead of this front aloft. This is demonstrated by separating the IWV into contributions from two layers (surface to 800 mb and 800 to 500 mb). The lower layer dried slightly northward from the surface front, but the upper layer moistened significantly. The analysis of  $q$  in Fig. 8a shows this well: for example, below 900 mb  $q$  decreased northward from its prefrontal maximum value of  $>10 \text{ g kg}^{-1}$ , while near 600 mb  $q$  increased from

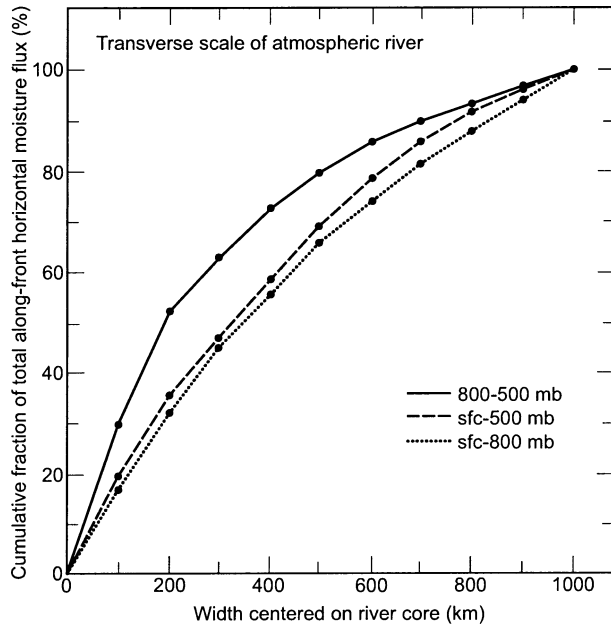


FIG. 10. Cumulative fraction (%) of total alongfront horizontal moisture flux for three layers (surface–500 mb, surface–800 mb, and 800–500 mb) centered on the core of the atmospheric river shown in Fig. 9.

$<1 \text{ g kg}^{-1}$  to  $>4 \text{ g kg}^{-1}$ . The upper layer (800–500 mb; see Fig. 8b) experienced a dramatic decrease in IWV behind the convection. Figure 8 clearly illustrates that the elongated front-parallel plume of maximum surface–500-mb IWV (see also Fig. 6) was not associated with the position of the southern surface front but reflected the deep moisture ahead of this front aloft. This accounts for the structural similarity between the plan-view IWV and 700-mb  $q$  analyses (Figs. 6 and 7b) and the difference between the plan-view  $q$  analyses at 700 and 1000 mb (Figs. 7b and 7a).

The deep prefrontal moisture plume in conjunction with the strong front-parallel flow ahead of the southern cold front resulted in an atmospheric river of enhanced horizontal water vapor transport oriented parallel to the front. This atmospheric river is analogous to those discussed by Zhu and Newell (1998), who concluded that four to five such rivers located around the hemisphere account for the total hemispheric meridional moisture flux. However, their analysis is based on global-scale model analyses that do not fully capture the narrow transverse scale of moist plumes such as the one documented here. The horizontal water vapor flux through the plane of the cross section in Fig. 8a was determined by layer averaging the dropsondes into 50-mb increments between 1000 and 500 mb before ingesting these data into a variant of the relationship used by Zhu and Newell (1998):

$$F_h = (\rho Uq) \times \Delta z \times \Delta L, \quad (1)$$

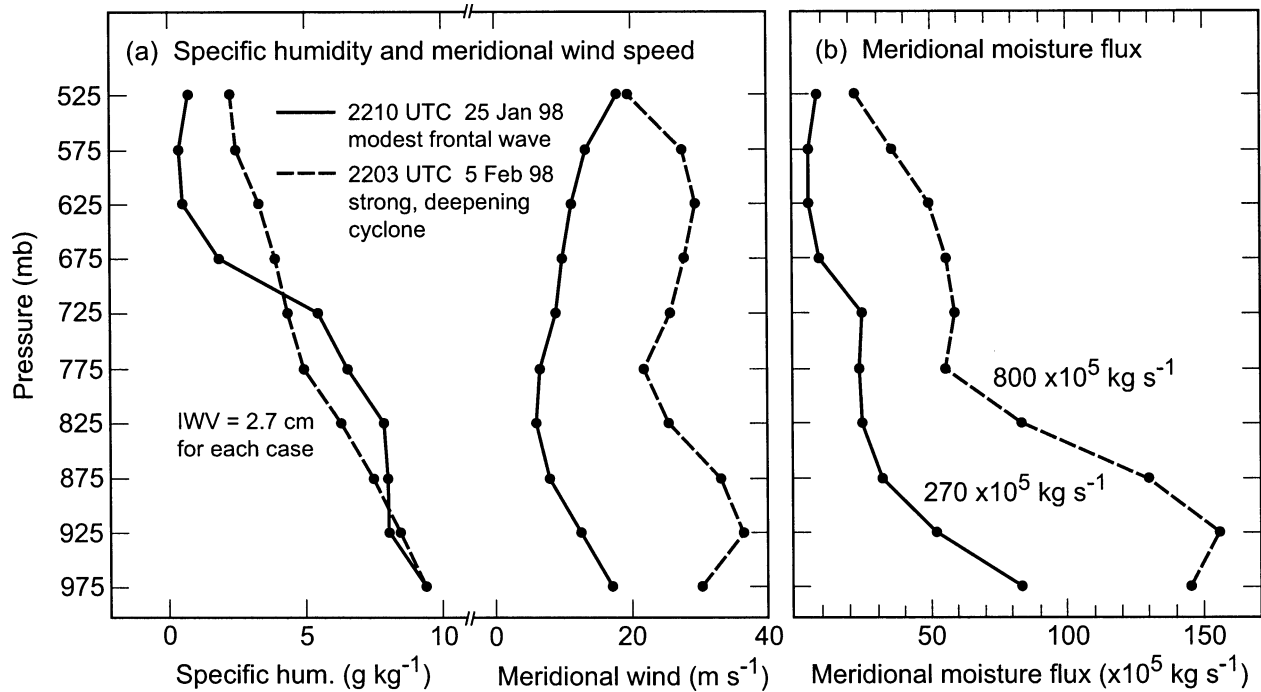


FIG. 11. Representative dropsonde profiles of (a) specific humidity ( $\text{g kg}^{-1}$ ) and meridional wind speed ( $\text{m s}^{-1}$ ) for the modest frontal wave of 25–26 Jan 1998 (solid curves) and for a strong, deepening cyclone on 5 Feb 1998 (dashed curves), and (b) meridional moisture flux ( $\times 10^5 \text{ kg s}^{-1}$ ) for the modest and strong events (solid and dashed curves, respectively), based on the curves in (a). The layer-integrated (1000–500 mb) meridional moisture flux values for the flux curves are shown in (b).

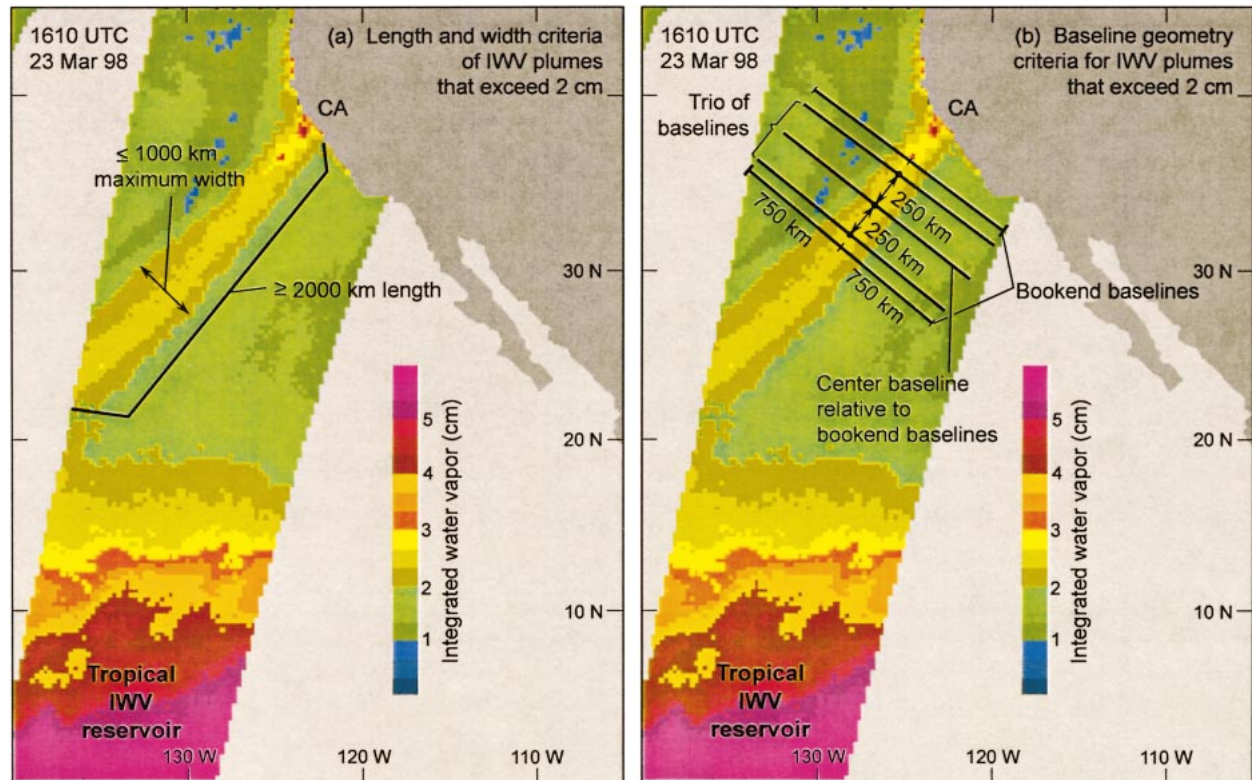


FIG. 12. Graphical depiction of the methodology employed to generate composite 1500-km-wide baselines of SSM/I-observed IWV, cloud liquid water, rain rate, and surface wind speed and GOES-observed cloud-top temperature and pressure across moisture plumes measured by SSM/I satellites over the eastern Pacific during the CALJET winter of 1997/98: (a) length and width criteria of IWV plumes that exceeded 2 cm, and (b) baseline geometry criteria relative to the SSM/I swaths for IWV plumes that exceeded 2 cm. The sample SSM/I image of IWV is from 1610 UTC 23 Mar 1998 during a flood-producing storm in coastal California (White et al. 2003).

where  $F_h$  is the alongfront horizontal water vapor flux (kilograms per second) in each 50-mb increment,  $\Delta z$  is the height range of each 50-mb increment, and  $\rho$ ,  $U$ , and  $q$  are the layer-mean values of air density, alongfront wind speed, and water vapor specific humidity within each 50-mb bin. Because the mean spacing between dropsondes in Fig. 8a is  $\sim 100$  km,  $\Delta L$  is also 100 km. The flux calculations for each dropsonde are assumed to be applicable in a 50-km window on either side of each dropsonde. An additional dropsonde at 2036 UTC 25 January and a rawinsonde at Vandenberg (VNB) at 0000 UTC 26 January 1998 were used to extend the cross section of  $F_h$  (Fig. 9a) southward beyond that shown in Fig. 8a in an effort to document the complete lateral extent of the atmospheric river.

Figure 9a shows a well-defined atmospheric river on the warm side of the southern cold front. Water vapor transport within this river exceeded  $80 \times 10^5 \text{ kg s}^{-1}$  within individual 50-mb bins below 800 mb, and the river extended up to  $\sim 600$  mb in the vicinity of the convection. A maximum value of  $>90 \times 10^5 \text{ kg s}^{-1}$  was observed near the southern front's LLJ. The northern cold front also possessed a local maximum of water vapor transport, though it was confined to a shallow layer below 800 mb. Traces of  $F_h$  along the cross section

are presented in Fig. 9b for three bulk layers (surface–500 mb, surface–800 mb, 800–500 mb), together with companion traces of IWV (see also Fig. 8b). In each bulk layer the character of the  $F_h$  trace mirrored that of the IWV. However, the  $F_h$  traces had a sharper peak associated with the atmospheric river, including that associated with the southern front's LLJ below 800 mb and that tied to the convection between 800 and 500 mb.

The transverse scale of this atmospheric river was assessed by determining the cumulative fraction of  $F_h$  along a 1000-km distance of the cross section, centered on the river core (Fig. 10). Between the surface and 500 mb, 75% of  $F_h$  was contained within the river in a swath only 565 km wide. In the upper portion of this layer between 800 and 500 mb, the same cumulative fraction was only 440 km wide. Six dropsondes in the core of the river where 75% of the surface–500-mb alongfront flux resided (2106 to 2253 UTC) possessed a meridional flux of  $1500 \times 10^5 \text{ kg s}^{-1}$ , or 20% of the global average across at  $35^\circ\text{N}$  reported in Zhu and Newell (1998). These in situ observations support Zhu and Newell's (1998) model-based conclusion that the hemispheric meridional moisture flux in the extratropics is accomplished almost entirely within narrow filaments. In our case the one

TABLE 1. A listing of the SSM/I and GOES baselines used in the satellite compositing analysis.

Date/time of SSM/I baseline trios for 1997/98 winter (overpass at 30°N)		Central SSM/I baseline information			Time offset between GOES and SSM/I (min)
MM/DD	Time (UTC)	Lat (°N)*	Lon (°W)*	Orienta-tion (°)**	
11/19	0255	33.56	125.48	325	—
11/20	0418	31.88	123.85	348	—
11/23	0224	25.15	132.59	331	—
11/23	0523	24.77	133.79	334	—
11/23	1452	25.69	131.40	334	—
11/23	1608	26.34	129.93	332	—
11/24	0212	27.10	128.63	330	—
11/24	1439	28.84	127.44	335	—
11/24	1554	30.09	124.89	339	—
12/02	0513	38.99	136.99	270	47
12/03	0203	29.98	130.21	314	—
12/03	0500	28.89	131.18	327	60
12/03	1728	28.89	128.03	311	32
12/04	1715	29.92	124.61	298	45
12/05	0139	28.84	123.64	303	—
12/05	0435	27.59	125.70	311	85
12/10	0515	40.40	140.63	302	45
12/30	0320	33.62	149.04	270	-20
12/30	0611	28.57	148.88	290	-11
12/30	1839	37.25	143.12	266	-39
12/31	0307	26.23	144.32	310	-7
12/31	0559	25.75	143.99	314	1
12/31	1535	25.26	142.85	318	—
01/07	0342	35.73	132.81	008	-42
01/10	1710	31.28	143.72	323	—
01/11	1502	35.90	131.89	335	—
01/12	0416	29.38	141.77	333	—
01/15	1744	33.62	151.38	327	16
01/15	1843	37.04	144.43	327	-43
01/16	0315	34.05	147.79	330	-15
01/16	0603	34.76	147.96	331	-3
01/16	1542	36.11	141.60	322	-42
01/16	1830	34.92	141.60	323	-30
01/17	0302	35.19	142.64	336	-2
01/17	0550	35.24	144.10	332	10
01/17	1818	37.96	137.26	291	-18
01/22	1857	27.05	150.34	320	-57
01/23	0331	24.66	149.37	329	—
01/24	0315	31.61	126.84	326	-15
01/25	0306	29.17	145.02	317	-6
01/25	1534	26.89	141.88	330	-34
01/25	1820	26.61	141.22	331	-20
01/26	0254	26.89	140.57	326	6
01/26	0430	24.99	143.07	329	—
01/26	0540	26.61	139.65	320	20
01/28	1643	36.01	131.40	292	77
01/31	0153	28.13	125.86	305	67
01/31	0504	32.42	152.03	331	—
02/01	0322	27.05	147.57	347	—
02/01	0607	26.89	146.54	346	—
02/01	1550	26.02	145.57	343	—
02/01	1717	25.31	146.43	336	—
02/01	1834	25.64	144.86	337	—
02/02	0310	24.88	143.45	322	—
02/02	0413	32.86	124.18	347	-73
02/02	0555	23.84	142.58	319	—
02/04	1513	35.19	133.63	302	-13
02/04	1637	34.59	133.30	307	83
02/04	1757	33.89	133.52	316	3

TABLE 1. (Continued)

Date/time of SSM/I baseline trios for 1997/98 winter (overpass at 30°N)		Central SSM/I baseline information			Time offset between GOES and SSM/I (min)
MM/DD	Time (UTC)	Lat (°N)*	Lon (°W)*	Orienta-tion (°)**	
02/05	0233	29.49	136.18	328	27
02/05	0517	29.92	135.04	326	43
02/06	0221	23.14	131.35	307	—
02/06	0342	23.25	130.86	311	—
02/06	0505	22.98	130.53	313	—
02/08	0155	28.30	127.49	328	65
02/08	0315	28.51	126.03	328	-15
02/08	0440	28.24	125.97	329	80
02/12	0403	30.63	139.81	323	-63
02/12	0532	30.41	138.39	327	28
02/12	1516	29.98	136.99	347	-16
02/12	1630	30.47	133.08	344	-90
02/12	1759	30.03	135.09	348	1
02/13	0237	29.76	136.39	356	23
02/13	0519	30.09	134.60	353	41
02/14	1452	29.38	130.69	333	8
02/14	1734	29.11	128.85	327	26
02/22	0228	30.20	134.93	333	32
02/22	0509	30.14	132.65	333	51
02/22	0509	30.03	132.76	334	51
03/01	0244	37.80	137.43	332	16
03/01	0336	37.36	137.64	333	-36
03/01	1512	37.20	133.08	328	-12
03/07	0313	28.57	146.22	329	-13
03/07	0550	30.20	143.40	328	10
03/07	1540	28.84	142.64	335	-40
03/07	1624	35.24	130.69	318	-84
03/07	1817	29.65	140.03	338	-17
03/08	0300	29.11	142.04	339	0
03/08	0343	31.12	132.21	348	-43
03/08	0537	29.76	139.22	347	23
03/08	1610	31.07	130.48	360	—
03/10	1503	34.92	132.05	319	-3
03/10	1740	37.53	128.47	316	20
03/11	1922	26.56	152.24	352	—
03/12	1439	33.83	126.62	302	—
03/14	0403	37.04	143.50	335	-63
03/14	1556	31.88	147.03	333	-56
03/14	1832	35.84	141.39	319	-32
03/15	0350	36.01	138.40	330	-50
03/22	0332	20.75	149.10	330	—
03/22	0606	22.70	145.24	320	—
03/22	1623	34.70	130.15	319	-83
03/23	1610	33.45	127.00	308	-70
03/24	1556	30.25	124.99	310	-56

\* The latitude and longitude values are valid for the center grid point of each central baseline.

\*\* The orientation represents the azimuth pointing angle on the cold side of each central baseline.

filament was roughly 600 km wide or ~1.8% of the earth's circumference at 35° latitude.

Depending on the strength and orientation of the tropospheric winds within a region of similarly high moisture content, the meridional water vapor flux can vary significantly. For example, Fig. 11a shows dropsonde

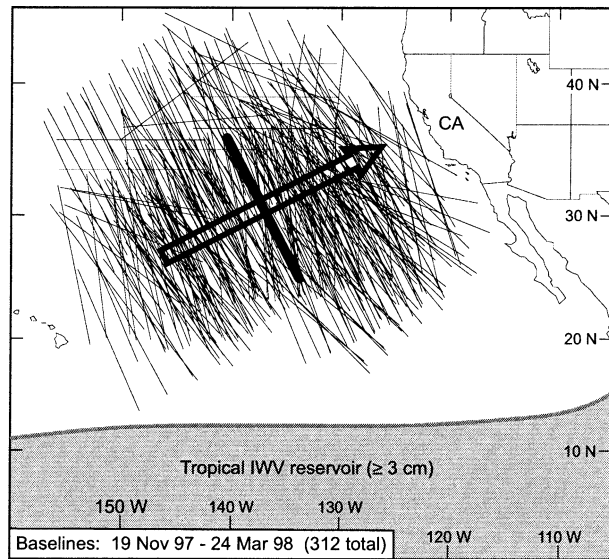


FIG. 13. The positions of all 312 baselines (thin lines) transecting 104 moisture plumes measured by SSM/I satellites between 19 Nov 1997 and 24 Mar 1998. These baselines were used to create the composite baseline (bold line) of SSM/I data. A 2000-km-long moisture plume (bold arrow) is depicted intersecting the composite baseline at a right angle. The tropical IWR reservoir ( $IWR \geq 3$  cm; shaded) is bounded by a solid gray-shaded line. The position of this line ( $IWR = 3$  cm) was determined from an average of every tenth daily IWR chart during the period of interest.

data from the cores of two atmospheric rivers, each with the same IWR content of 2.7 cm. The dropsonde on 25 January observed relatively weak meridional flow of less than  $18 \text{ m s}^{-1}$  within the modest frontal zone, while the dropsonde on 5 February measured strong meridional flow approaching  $40 \text{ m s}^{-1}$  within an intense cyclone. The resulting meridional moisture-flux profiles were therefore quite different for these two cases (Fig. 11b), assuming each sounding was representative of conditions in a 100-km-wide swath. The total surface–500-mb meridional flux was 3 times greater for the strong cyclone than for the modest front even though the IWR was the same. Yet, the weaker of these systems was still strong enough to account for a substantial fraction of the meridional fluxes across the earth's midlatitude belt (Zhu and Newell 1998).

#### 4. Winter-season satellite analysis of moisture plumes over the eastern Pacific

The case study of the IWR plume (Fig. 6) and its atmospheric river (Fig. 9) on 26 January highlights the river's transverse characteristics, vertical structure, and elongated nature. While the overall horizontal water vapor flux magnitude of this event matches the model-derived value that Zhu and Newell (1998) suggested is typical of an individual atmospheric river, it is possible that the detailed case study was not characteristic of most atmospheric rivers. Thus, it is important to assess

the representativeness of this single case using observations that can quantitatively document at least one key aspect of most atmospheric rivers. The combination of polar-orbiting and geostationary satellite observations provides the suitable spatiotemporal coverage for this purpose. However, because satellites are unable to directly observe  $F_h$  (sections 4b and 4c), the analysis focuses on other key signatures of atmospheric rivers, that is, patterns of IWR and other satellite-derived products such as CLW, RR, CTT, and CTP. The use of IWR as a proxy for determining the positions and widths of atmospheric rivers is based upon the close correlation between IWR and vertically integrated horizontal water vapor fluxes shown in the case study and on the general connection that is to be expected between these variables in extratropical cyclones. Henceforth, the term atmospheric rivers will be used when discussing the satellite-derived IWR results. The procedure used in section 4a to identify cases focuses on narrow, elongated IWR features exceeding 2-cm IWR. All SSM/I IWR images over the eastern Pacific during the CALJET winter of 1997/98 were examined for the presence of narrow plumes of high IWR. Representative transects oriented orthogonal to those plumes that met objective geometric criteria (section 4a) were then synthesized into a composite 1500-km-wide transverse baseline of SSM/I-observed IWR, CLW, RR, and SPD. GOES-observed CTT, CTP, and IWR along these same baselines were then also calculated. Events meeting the objective criteria were identified on 46 dates during the same winter as the case study.

##### a. Compositing methodology using SSM/I and GOES observations

The winter-season satellite analysis of elongated tropospheric moisture plumes over the eastern Pacific during CALJET encompassed a 137-day period between 15 November 1997 and 31 March 1998 in a domain bounded by  $0^\circ$ – $45^\circ\text{N}$  latitude and  $105^\circ$ – $160^\circ\text{W}$  longitude. The initial analysis step for generating a composite cross-plume baseline required the perusal of daily averaged plan-view images of SSM/I-observed IWR for moisture plumes whose core values exceeded 2 cm for  $\geq 2000$  km in the along-plume direction and  $\leq 1000$  km in the cross-plume direction. Because the daily averaged images covered the entire eastern Pacific, the selection methodology allowed identification of IWR plumes of any orientation. The threshold of 2 cm was chosen because the atmospheric river in Fig. 9a was roughly bounded by  $IWR = 2$  cm. For those days when moisture plumes conformed to the aforementioned dimensions, the individual SSM/I IWR orbital swaths that composed the daily averages were then inspected to ascertain if these plumes were authentic (e.g., Fig. 12a). (Readily identifiable artifacts in these daily maps can arise because of averaging that was applied when there was spatial overlap from overpasses that occurred at differ-

ent times during the same day. However, the analyses presented henceforth are based entirely on the individual orbital swaths and thus are not affected by this averaging.) Using this methodology, 175 individual SSM/I images possessed an elongated ( $\geq 2000$  km  $\times$   $\leq 1000$  km) moisture plume exceeding 2 cm on 58 out of 137 days, that is, on 42% of the days.

Figure 12b highlights the next set of steps that was implemented to create a composite transverse baseline orthogonal to the IWV plumes. To ensure that the composite baseline extended well beyond the narrow ( $\leq 1000$  km) corridor of  $IWV \geq 2$  cm, individual baselines that made up the composite were required to span 750 km on each side of the plume core. For each of the 175 SSM/I images, a pair of 1500-km-long "bookend" baselines were first determined, based on the orientation of the  $\sim 1400$ -km-wide satellite swath relative to the IWV plume. The bookend baselines were positioned such that their centers resided in the core of the IWV plume, they were oriented perpendicular to the plume, and one end of each baseline terminated at the edge of the satellite swath. If the distance between the bookend baselines in the core of the IWV plume exceeded 500 km, then a center baseline was cut orthogonal to the IWV plume midway between the bookend baselines. Then, two more baselines were cut orthogonal to the plume 250 km on each side of the center baseline. Each trio of baselines enclosed by the bookend baselines were then used in the subsequent SSM/I compositing of IWV, CLW, RR, and SPD. These baselines possessed a 25-km grid spacing that is only slightly smaller than the native resolution of the SSM/I observations. Using trios of baselines in a 500-km along-plume segment ensures that representative sampling across each moisture plume was obtained. These additional criteria reduced the number of days and images with elongated IWV plumes to 46 and 104, respectively. Hence, the composite SSM/I baselines of IWV, CLW, RR, and SPD are each composed of 312 individual transects. The time, position, and orientation of the central baseline of each triplet are provided in Table 1.

The locations of all 312 baselines are shown in Fig. 13 within the satellite analysis domain. These baselines reside in the midlatitudes north of the tropical moisture reservoir where  $IWV \geq 3$  cm. The reservoir's north wall migrated systematically southward during the winter. The position of the 1500-km-wide composite baseline is also shown in Fig. 13. The composite possesses a northwest-to-southeast orientation of  $325^\circ$  (cold) to  $145^\circ$  (warm), thus revealing that the mean moisture plume was directed from southwest to northeast toward California.

In an effort to place the composite baseline into synoptic-scale context, composite plan-view analyses were generated using daily global gridded data from the National Centers for Environmental Prediction–National Center for Atmospheric Research (NCEP–NCAR) reanalysis project (e.g., Kalnay et al. 1996). Those days

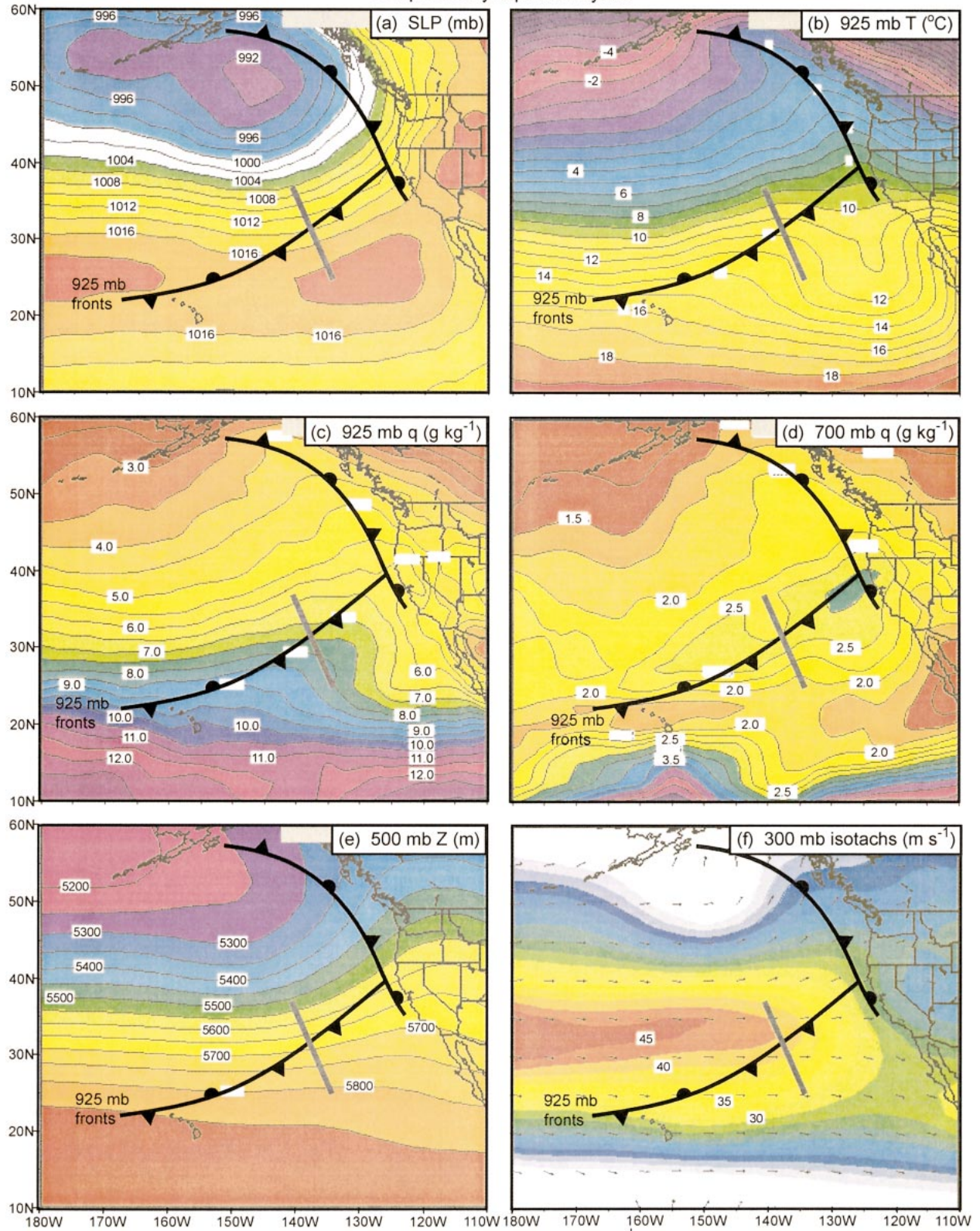
with at least one suitable SSM/I IWV swath from which baseline trios were obtained (46 days total) were included in the synoptic compositing (Fig. 14). Although the coarse grid spacing of the NCEP–NCAR fields ( $2.5^\circ$  latitude by  $2.5^\circ$  longitude) could not resolve the narrow atmospheric rivers themselves, the synoptic composites do provide the large-scale context. Specifically, the composite baseline resided south of a deeply occluded cyclone over the Gulf of Alaska, crossed a warm and moist axis at 925 mb, transected an isolated and elongated region of large specific humidity at 700 mb, was downstream of the mean 500-mb trough position (without exception, the SSM/I IWV plumes that were the basis for the synoptic composites were situated on the downstream side of 500-mb extratropical trough axes), and resided in the right exit region of a 300-mb jet. To further define the synoptic context, approximate frontal positions (shown in Fig. 14) were derived from distinct features in the 925-mb thermal and specific humidity fields. This synoptic compositing and frontal analysis places the composite baseline nearly orthogonal to the 925-mb polar cold-frontal zone and indicates that the composite SSM/I IWV maximum at the midpoint of the baseline was located in the cyclone warm sector, as was also true in the detailed case study of 26 January 1998 (section 3). Based on the composite analysis results, the IWV plumes were found within warm conveyor belts of extratropical cyclones (e.g., Browning 1990; Carlson 1991). Although it is theoretically possible for an elongated IWV plume to exist without it marking an atmospheric river, such as in a col region of weak wind, the synoptic compositing places the events studied here in a large-scale setting where these conditions are extremely unlikely to occur.

We assessed the cloud-top temperature and pressure characteristics across these moisture plumes by creating composite baselines of CTT and CTP from GOES data that were available north of  $\sim 22^\circ$ N latitude on a 3-h basis from 1 December 1997 to 31 March 1998. A composite baseline of GOES IWV was also synthesized. The positions of the individual baselines used to create the SSM/I cross-plume composites were also used to create the companion GOES composites, provided the time difference between SSM/I and corresponding GOES images was less than 1.5 h. Because of the smaller spatial window of GOES data availability relative to the SSM/I observations, the GOES composites of CTT, CTP, and IWV contain only 196 samples rather than 312. The average time difference between the 196 GOES images and companion SSM/I images is only  $-3.2$  min, with a standard deviation of 43.1 min. Table 1 indicates which samples were used to create the GOES composites. To make meaningful comparisons between the SSM/I and GOES composites, 196-sample subset composites of the SSM/I data were also constructed.

#### b. SSM/I composite results

The SSM/I-observed composite baseline of IWV constructed from the 312 transects with  $IWV \geq 2$  cm is

Composite Synoptic Analyses



shown in Fig. 15a. The mean and standard deviation of the width scale of IWV that exceeds 2 cm is  $388 \pm 121$  km, which is similar to the 424-km width scale observed in the case study and much narrower than the 1000-km cross-plume criterion that was employed. Two subset composite baselines of IWV were synthesized from the 312 transects and are also presented in Fig. 15a. These subset composites are composed of transects whose core regions of IWV exceeded 3 and 4 cm, and their respective sample sizes are 84 and 9 (i.e., 27% and 9% of 312, respectively). The 2+, 3+, and 4+ cm traces contain peak values of 2.81, 3.41, and 4.19 cm, respectively (Table 2), and the peak value of the 4+ cm trace is 49% larger than that of the 2+ cm trace. However, >200 km beyond the core region, the IWV values of these composite traces are quite similar. Thus, the magnitude of IWV within the core of the moisture plumes is not well correlated with IWV content outside the plume cores. As expected, the endpoints or wings of these composite traces show a poleward decrease in the background moisture content.

Companion composite traces of CLW and RR (Figs. 15b and 15c) show well-defined peak values in the core of the 2+, 3+, and 4+ cm composite IWV plumes (Table 2 lists these values). The peak value of CLW in the 2+ and 4+ cm IWV traces increases by 192%, even though the corresponding IWV peak increases by only 49%. The peak value of RR increases by an even larger 463%. Hence, from a statistical perspective, a relatively modest increase of IWV within the core of a moisture plume yields a much more substantial increase in the corresponding cloud liquid water and rain-rate peaks. This suggests that nonlinear processes, such as those driving vertical circulations associated with fronts and/or convection, are enhanced in IWV plumes with greater moisture content. The wings of the CLW and RR traces possess a background trend opposite to that observed in the IWV traces. The larger values of CLW and RR on the northern wing quite likely reflect the presence of slantwise baroclinic ascent on the cold side of the IWV plumes.

The narrow transverse character of the composite IWV traces was quantified by calculating the cumulative fraction of the IWV perturbation centered on the plume core.<sup>2</sup> This analysis was repeated for the composite

CLW and RR traces. For the average of the three composite IWV traces, ~75% of the perturbation to the background IWV is contained in a narrow region 417.3 km wide (Fig. 15d; Table 3). It is noteworthy that this width is independent of the core value of IWV (Table 3). Roughly 75% of the perturbation to the background CLW and RR is contained in even narrower ribbons only 175.7 and 140.7 km wide, respectively (Figs. 15e and 15f; Table 3). The difference in width scale between the IWV traces and the CLW and RR traces suggests that processes leading to the development of moisture plumes operate on a much larger scale than those responsible for the generation of cloud liquid water and rainfall. Based on preliminary numerical model results (not shown), the primarily geostrophic horizontal frontal confluence contributes significantly to the development of IWV plumes, and ageostrophic secondary vertical frontal circulations focus the narrower CLW and RR peaks within these plumes. A detailed examination of these numerical results will be the focus of a future study.

Because rainfall is often observed within elongated IWV plumes but interferes with SSM/I-based wind retrievals, the SPD coverage in this important region is deficient (Fig. 16a). Only 25% of SPD measurements in the core of the 2+ cm IWV composite trace were deemed reliable by the SSM/I retrieval algorithm. A 310-km window of <80% SPD coverage straddles the plume core (Fig. 16b), corresponding to a composite CLW of  $\geq 0.08 \text{ kg m}^{-2}$ . The asymmetric position of this window relative to the IWV core reflects the prevalence of rainfall on the cold side of the core and the likelihood that slantwise baroclinic ascent played a role in this cold-side bias. The percentage of successful SPD retrievals decreased to 18% and 0% in the core of the 3+ and 4+ cm plumes, respectively, thus revealing that rainfall and its detrimental impact on the SPD retrievals are more prevalent in moisture plumes with greater IWV content.

Composite traces of IWV and CLW composed of individual transects where no rain was observed (i.e., those traces composed entirely of valid SPD observations—a subsample of 35) are compared to their 312-sample counterparts (i.e., the 2+ cm IWV plumes; Fig. 17a). The composite IWV trace with valid SPD observations mirrors the 2+ cm trace, but the composite CLW trace composed of valid SPD data is quite different. Namely, the peak value of  $\sim 0.08 \text{ kg m}^{-2}$  within the CLW subsample composite is 1/6 the magnitude of CLW corresponding to the 2+ cm trace, and this value

<sup>2</sup> The total perturbation is defined by the area bounded beneath the IWV curve and above a linear-trend line connecting the endpoints of this curve. Fractional perturbation elements are 50 km wide centered on the plume core, and they are also bounded by the curve and trend line.

←

FIG. 14. Composite analyses based on the NCEP–NCAR daily reanalysis global gridded dataset for the 46 days with baselines shown in Fig. 13: (a) SLP (mb), (b) 925-mb temperature ( $T$ ; °C), (c) 925-mb specific humidity ( $q$ ;  $\text{g kg}^{-1}$ ), (d) 700-mb specific humidity ( $q$ ;  $\text{g kg}^{-1}$ ), (e) 500-mb geopotential height ( $Z$ ; m), and (f) 300-mb isotachs ( $\text{m s}^{-1}$ ) and wind vectors. Frontal interpretations are based on the composite analyses. Standard frontal notation is used. The bold gray line transecting the cold front in each panel is the composite baseline shown in Fig. 13.

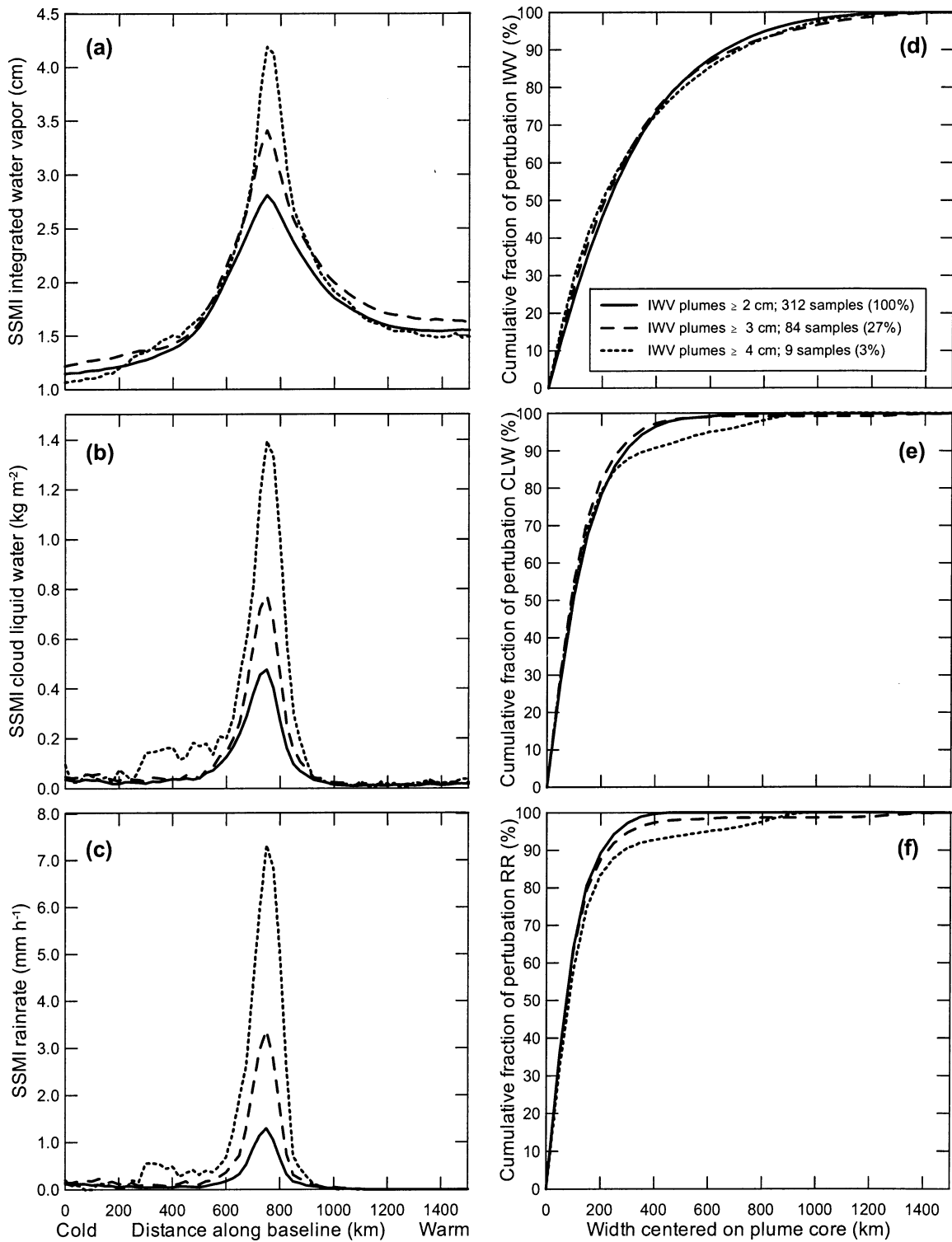


FIG. 15. Composite SSM/I-observed baselines of (a) IWV (cm), (b) CLW ( $\text{kg m}^{-2}$ ), and (c) RR ( $\text{mm h}^{-1}$ ) across those moisture plumes containing  $\geq 2$  cm (solid line),  $\geq 3$  cm (dashed line), and  $\geq 4$  cm (dotted line) of IWV observed by SSM/I. Cumulative fraction (%) of perturbation (d) IWV, (e) CLW, and (f) RR, centered on the core of the composite of SSM/I-observed moisture plumes containing  $\geq 2$ ,  $\geq 3$ , and  $\geq 4$  cm of IWV.

TABLE 2. Maximum mean values of SSM/I-observed IWV (cm), CLW ( $\text{kg m}^{-2}$ ), and RR ( $\text{mm h}^{-1}$ ), and minimum mean values of GOES-observed CTT (K) and CTP (mb) in the core of the composite moisture plumes containing greater than 2, 3, and 4 cm of IWV observed by SSM/I. The sample sizes used to obtain the mean values are also provided.

Composite IWV core magnitude	SSM/I observations			Sample size	GOES observations		
	IWV (cm)	CLW ( $\text{kg m}^{-2}$ )	RR ( $\text{mm h}^{-1}$ )		CTT (K)	CTP (mb)	Sample size
2+ cm plumes	2.81	0.48	1.30	312	251.4	481.2	196
3+ cm plumes	3.41	0.77	3.38	84	244.1	392.1	52
4+ cm plumes	4.19	1.40	7.32	9	235.3	321.7	9

is consistent with the CLW threshold shown in Fig. 16b. A composite trace of SPD derived from the 35-transect subsample (Fig. 17b) contains a modest wind speed maximum of  $6.4 \text{ m s}^{-1}$  within the core of the composite IWV plume. Using the case-study results as a guide, this maximum represents a pre-cold-frontal LLJ. A second composite SPD trace, composed of individual transects whose core IWV values exceed 4 cm (Fig. 17b), contains a stronger LLJ perturbation and stronger winds overall, but the SPD values are missing in the core. A comparison of these traces suggests that moisture plumes with a larger IWV content are accompanied by stronger winds and, therefore, a nonlinear increase in horizontal moisture flux. However, because the SSM/I SPD retrievals are degraded in rainfall, and rainfall is commonly observed in elongated moisture plumes (especially in plumes accompanied by stronger surface winds), the combined SSM/I dataset of IWV and SPD cannot provide reliable low-level horizontal water vapor flux estimates within these plumes.

c. GOES composite results

To assess the cloud-top temperature and pressure characteristics across the moisture plumes described above, composite baselines of GOES CTT and CTP were constructed when concurrent GOES and SSM/I data were available, that is, from 196 transects north of  $22^\circ\text{N}$  latitude between 1 December 1997 and 31 March 1998. Composite traces of SSM/I-observed IWV and CLW for this 196-transect subsample (where the core value of IWV in each transect exceeded  $<2$  cm) bear a striking resemblance to their 312-transect counterparts (Fig. 18a), except for slightly lower values of IWV at the wings and a slightly higher value of CLW in the

TABLE 3. Width scales (km) of the 75% cumulative fraction of perturbation IWV, CLW, and RR across those composite moisture plumes containing greater than 2, 3, and 4 cm of IWV observed by SSM/I. The average width scales are also shown.

Composite IWV core magnitude	Width scale (km) for 75% cumulative fraction		
	IWV	CLW	RR
2+ cm plumes	415.6	184.3	133.4
3+ cm plumes	408.9	164.5	136.6
4+ cm plumes	427.3	178.4	152.0
Average	417.3	175.7	140.7

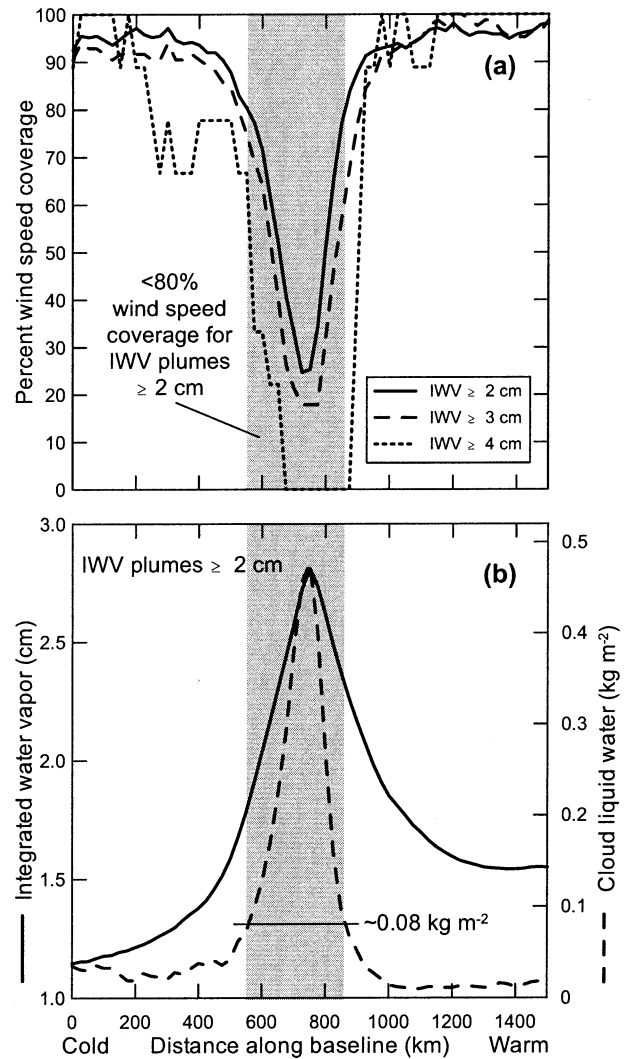


FIG. 16. (a) Percent wind speed coverage (observed by SSM/I) across those moisture plumes containing  $\geq 2$  cm (solid line),  $\geq 3$  cm (dashed line), and  $\geq 4$  cm (dotted line) of SSM/I-observed IWV. (b) Composite baselines of IWV (solid; cm) and CLW (dashed;  $\text{kg m}^{-2}$ ) across those moisture plumes containing  $\geq 2$  cm of SSM/I-observed IWV. The gray-shaded bars correspond to the width scale of SSM/I observations with  $<80\%$  wind speed coverage for IWV plumes  $\geq 2$  cm.

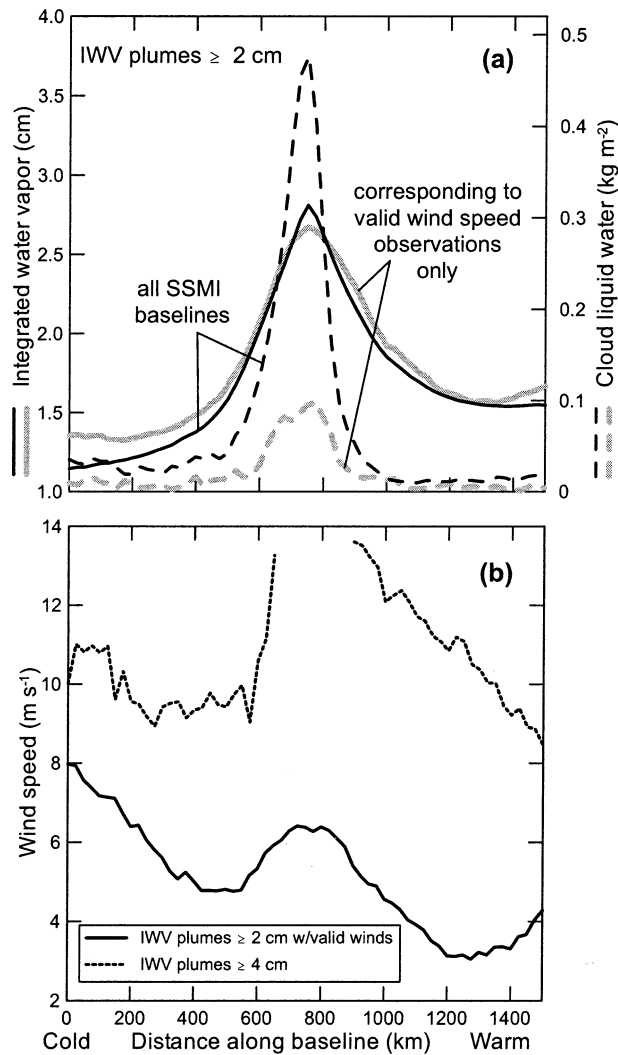


FIG. 17. (a) Composite baselines of I WV (solid lines, cm; observed by SSM/I) and CLW (dashed lines,  $\text{kg m}^{-2}$ ; observed by SSM/I) across all moisture plumes containing  $\geq 2$  cm of SSM/I-observed I WV (black lines), and across those moisture plumes containing  $\geq 2$  cm of SSM/I-observed I WV with valid SSM/I-observed wind speed observations (gray shaded lines). (b) Composite baselines of wind speed ( $\text{m s}^{-1}$ ; observed by SSM/I) across those moisture plumes containing  $\geq 2$  cm of SSM/I-observed I WV with valid wind speed observations (solid), and across those moisture plumes containing  $\geq 4$  cm of SSM/I-observed I WV (dashed; the broken portion of the curve is where no wind speed data were available from any of the individual transects).

core. These minor differences arose due to the latitudinal dependence of the compositing results (see section 4d), since the southernmost transects that make up the 312-sample composites were not included in the 196-sample composites because of the absence of GOES data south of  $22^{\circ}\text{N}$ . Because the 196- and 312-sample composites are so similar (as are the composites corresponding to the 3+ and 4+ cm I WV plumes; not shown), meaningful comparisons can be made between the GOES and SSM/I results.

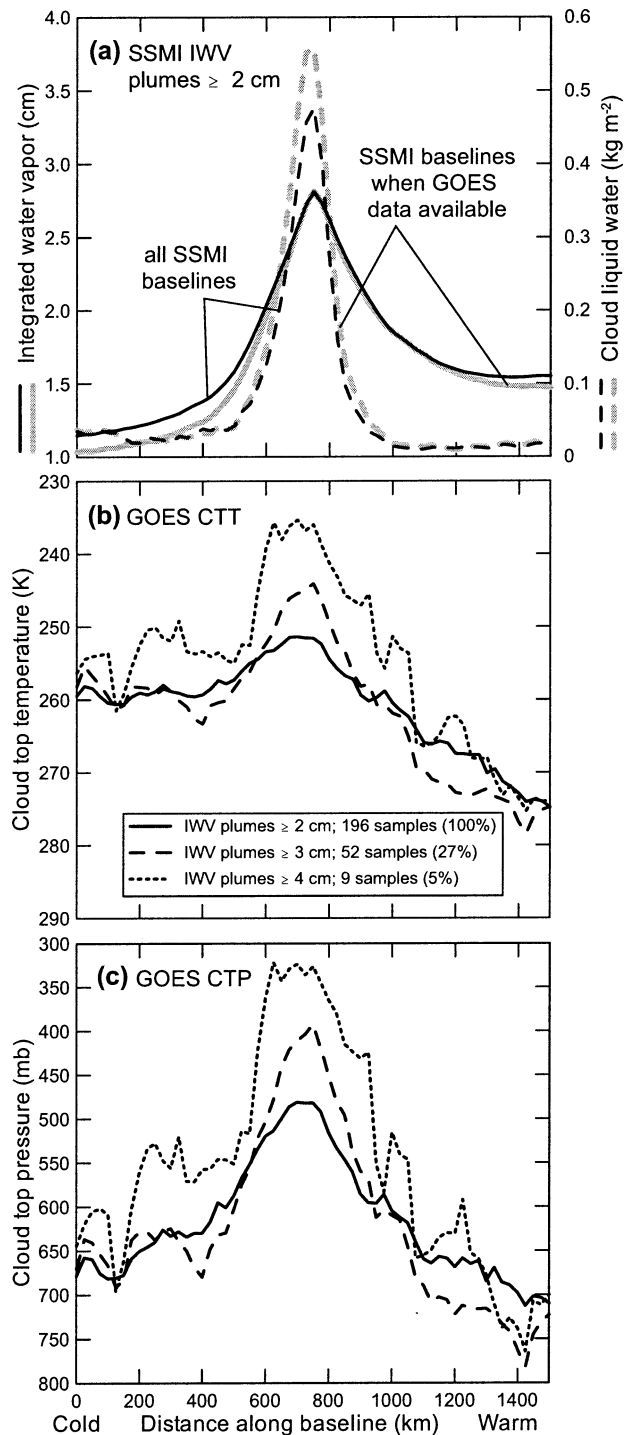


FIG. 18. (a) Composite baselines of I WV (solid lines, cm; observed by SSM/I) and CLW (dashed lines,  $\text{kg m}^{-2}$ ; observed by SSM/I) across all moisture plumes containing  $\geq 2$  cm of SSM/I-observed I WV (black lines), and across those moisture plumes containing  $\geq 2$  cm of SSM/I-observed I WV when GOES data were also available (gray shaded lines). (b), (c) Composite baselines of CTT (K; observed by GOES) and CTP (mb; observed by GOES) across those moisture plumes containing  $\geq 2$  cm (solid line),  $\geq 3$  cm (dashed line), and  $\geq 4$  cm (dotted line) of SSM/I-observed I WV.

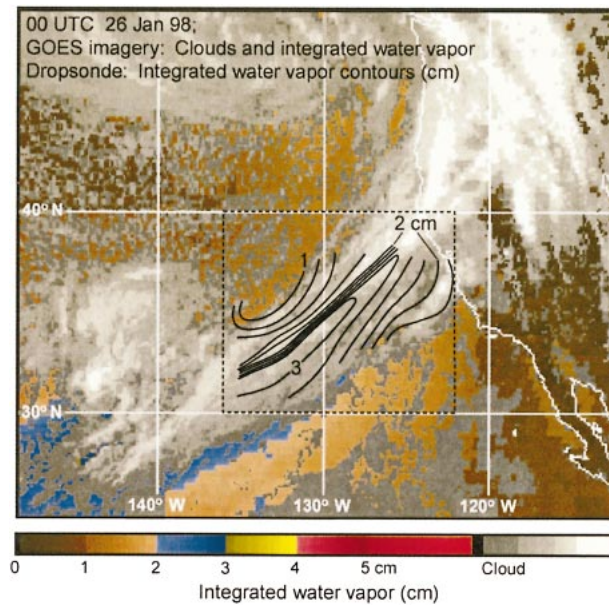


FIG. 19. GOES satellite image of IWV (cm; color coded) and clouds at 0000 UTC 26 Jan 1998. The dropsonde-derived IWV analysis within the dashed inset box (see Fig. 6) is overlaid.

Composite traces of GOES CTT and CTP (Figs. 18b and 18c) show that the coldest and deepest cloud tops are situated in the core of the IWV plumes. In addition, the cloud tops become substantially colder and deeper within the core of the IWV plumes when the moisture content within these plumes increases (see also Table 2). Specifically, the core value of CTT decreases from 251.4 K in the 2+ cm composite IWV trace to 235.3 K in the 4+ cm trace, and the corresponding core value of CTP decreases from 481.2 to 321.7 mb between the 2+ and 4+ cm composite traces. The anticorrelation between the core moisture content in the composite IWV plumes and the embedded cloud-top core values may arise, at least in part, because of latent heating: as the moisture content within IWV plumes increases, latent heating triggered by forced ascent will be more vigorous, resulting in enhanced upward motion and saturated conditions deeper in the troposphere. Those plumes with greater moisture content may also be indicative of stronger and deeper baroclinic zones and attendant vertical circulations that cause saturated conditions deeper into the troposphere. The wings of the composite CTT trace contain a poleward decrease in cloud-top temperature of  $\sim 17$  K, quite likely reflecting the background decrease of temperature with latitude.

Because elongated moisture plumes represent regions of deep cloudiness, the GOES satellites do not provide reliable IWV retrievals there, despite the excellent spatiotemporal coverage of the GOES IWV data in cloud-free regions. For example, the GOES satellite image and superimposed dropsonde-based IWV analysis at 0000 UTC 26 January 1998 (Fig. 19) reveal a narrow plume of enhanced IWV ( $>3$  cm in a swath  $<100$  km wide)

associated with an atmospheric river residing beneath the cold-frontal cloud band. These clouds hide the core of the moisture plume from the GOES retrievals, which see at most 2.2 cm of IWV at the periphery of this region. Thus, in this case the core of the moisture plume had IWV values 40% greater than those seen by the GOES retrieval. From a statistical perspective, the composite baselines of GOES IWV data for the 2+, 3+, and 4+ cm SSM/I-observed IWV plumes have 0% GOES coverage in the core of the composite moisture plumes (Fig. 20a), and the width scale of the data void in the core region expands with increasing moisture content. Hence, there is no GOES IWV coverage within the core region of the narrow moisture plumes or atmospheric rivers, and even the wings of the composite traces are characterized by GOES IWV coverage of only  $\sim 25\%$ – $55\%$ .

To explore if the GOES IWV retrievals at the periphery of moisture plumes are able to help determine the moisture content within the core of those plumes, an autocorrelation analysis was performed on the 312 SSM/I transects that make up the 2+ cm composite IWV trace. Specifically, a correlation analysis was carried out between the 312 IWV observations at the center or core grid point at  $X = 750$  km and the 312 IWV measurements at each of the 61 grid points from  $X = 0$  km to  $X = 1500$  km. The results are presented in Fig. 20b and show a narrow region of large autocorrelation cradled within the envelope of poor GOES IWV coverage (Fig. 20a). Significantly, the maximum IWV value that characterizes a moisture plume or atmospheric river is nearly uncorrelated with values just 200 km away from the core. This has important implications not only for the operational nowcasting use of GOES IWV in the vicinity of moisture plumes, but also for utilizing GOES IWV data in numerical model initializations and data assimilation. However, the GOES CTT and CTP results suggest that the correlations between CTT, CTP, and IWV could prove to be operationally valuable. In an effort to help fill this gap in GOES IWV coverage, Scofield et al. (2000) developed a composite precipitable water vapor product that takes advantage of both GOES and SSM/I satellite datasets as well as operational global-scale numerical model analyses of water vapor. However, this composite product has not been evaluated here.

#### d. Characteristics of atmospheric rivers as a function of latitude

The winter-season satellite analysis and case study have documented fundamental transverse characteristics of elongated moisture plumes and associated atmospheric rivers. In an effort to also ascertain key along-plume characteristics, the impact of latitude on moisture plumes was evaluated by generating composite SSM/I and GOES baselines based on the latitude of the center grid point of each of the 312 transects. The individual transects were grouped into four  $5^\circ$  wide latitude bins

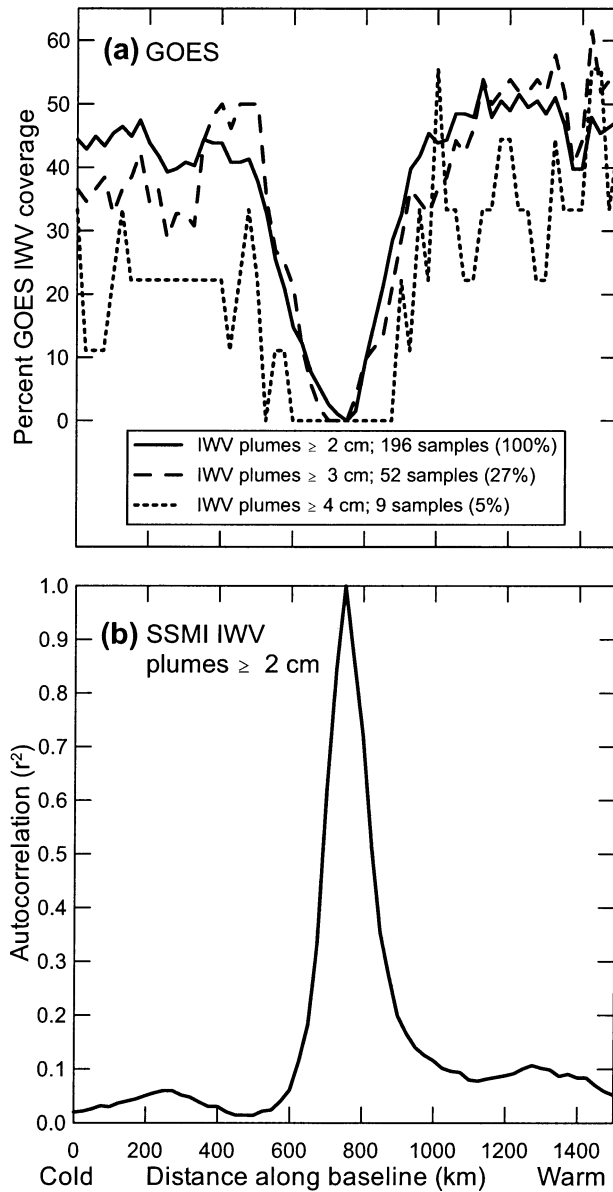


FIG. 20. (a) Percent IWV coverage (observed by GOES) across those moisture plumes containing  $\geq 2$  cm (solid line),  $\geq 3$  cm (dashed line), and  $\geq 4$  cm (dotted line) of SSM/I-observed IWV. (b) Autocorrelation between the peak SSM/I-observed IWV value (i.e., the center grid point) from each of the 312 baselines and the IWV value at each 25-km resolution grid point from each of these baselines.

(i.e.,  $20^{\circ}$ – $25^{\circ}$ N,  $25^{\circ}$ – $30^{\circ}$ N,  $30^{\circ}$ – $35^{\circ}$ N, and  $35^{\circ}$ – $40^{\circ}$ N), and the composite baselines were then created from these transects for each bin. The mean orientation of these baselines does not change appreciably with increasing latitude (ranging from  $316^{\circ}$ – $136^{\circ}$  to  $329^{\circ}$ – $149^{\circ}$ ), and they mirror the orientation of the 312-transect composite baseline for SSM/I IWV  $\geq 2$  cm ( $325^{\circ}$ – $145^{\circ}$ ). Because GOES data were not available south of  $22^{\circ}$ N, we were unable to construct GOES composites for the southernmost bin.

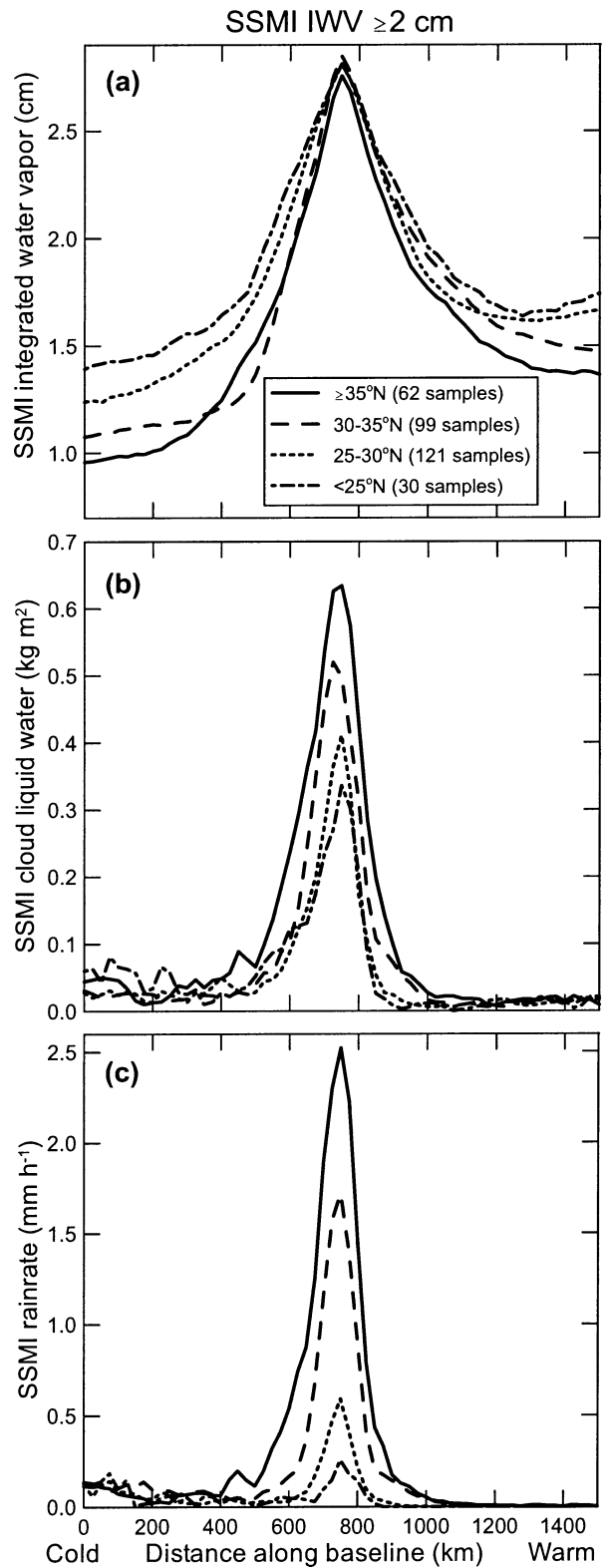


FIG. 21. Composite baselines of SSM/I-observed (a) IWV (cm), (b) CLW ( $\text{kg m}^{-2}$ ), and (c) RR ( $\text{mm h}^{-1}$ ), across all moisture plumes containing  $\geq 2$  cm of SSM/I-observed IWV within four discrete latitude bins (latitudes  $\geq 35^{\circ}$ N, solid;  $30^{\circ}$ – $35^{\circ}$ N, dashed;  $25^{\circ}$ – $30^{\circ}$ N, dot-dash;  $<25^{\circ}$ N, dot-dash).

TABLE 4. Maximum mean values of SSM/I-observed IWV (cm), CLW ( $\text{kg m}^{-2}$ ), and RR ( $\text{mm h}^{-1}$ ), and minimum mean values of GOES-observed CTT (K) and CTP (mb) as a function of latitude in the core of the composite moisture plumes containing greater than 2 cm of IWV observed by SSM/I. The sample sizes used to obtain the mean values are also provided.

Latitude bin	SSM/I observations				GOES observations		
	IWV (cm)	CLW ( $\text{kg m}^{-2}$ )	RR ( $\text{mm h}^{-1}$ )	Sample size	CTT (K)	CTP (mb)	Sample size
<25°N	2.81	0.34	0.26	30	—	—	0
25°–30°N	2.81	0.41	0.59	121	259.5	579.2	61
30°–35°N	2.85	0.52	1.72	99	251.5	475.1	76
35°–40°N	2.76	0.63	2.52	62	240.2	379.6	59

The peak moisture content within the core of the SSM/I IWV composites (Fig. 21a) does not vary appreciably between 20° and 40°N; an average peak value of  $2.81 \pm 0.04$  cm is observed (see also Table 4). However, the width scale of IWV that exceeds 2 cm in these composites decreases systematically from south to north from 449.8 to 298.0 km (Table 5). Because the case study and synoptic compositing imply that elongated moisture plumes coincide with frontal zones, the northward decrease in width scale suggests that frontal confluence may act to contract the lateral scale of the IWV plumes with increasing distance downstream of the southern terminus of the fronts. The IWV content in each wing of these composites decreases systematically with increasing latitude, thus documenting the northward decrease in background water vapor. The CLW and RR composite traces (Figs. 21b and 21c) show latitudinal variations primarily within the core of the moisture plumes. Specifically, the peak value of CLW in the core region increases by nearly a factor of 2 between the southernmost and northernmost baselines, while the peak value of RR increases by an order of magnitude from south to north (see also Table 4). In addition, the width scale of CLW and RR increases with increasing latitude (see also Table 5), opposite that of the composite IWV traces. These CLW and RR characteristics reflect the fact that frontal circulations are generally stronger and broader in the midlatitude storm track than they are in the subtropics. Jet dynamics may have played a role in the latitudinal dependence of CLW and RR, given that the more southern moist-plume transects were quite likely located in the often subsident right exit region (Keyser and Shapiro 1986) of quasi-linear jet streams (see Fig. 14f) where cloud formation and rainfall were

suppressed. Finally, the latitudinal variation of CLW and RR may be partly attributable to Hadley cell subsidence, which can extend northward to  $\sim 30^\circ\text{N}$  in the Northern Hemispheric winter mean (Peixoto and Oort 1992, 157–159), thus preferentially impacting the southernmost moist-plume transects.

The GOES composite traces of CTT (Fig. 22a) show a systematic northward decrease in cloud-top temperature across these traces southeast of  $X \approx 250$  km that partly reflects the poleward decrease in temperature. Significantly, a northward increase in the cold cloud-top perturbation within the core of the moisture plumes is also observed across these traces. The northernmost composite, which possesses a core CTT value of 240.2 K, is characterized by a well-defined cold perturbation of 15–20 K. In contrast, the core of the southernmost composite is nearly 20 K warmer (see also Table 4) and does not exhibit a substantive cold perturbation. Hence, elongated moisture plumes are more easily distinguishable using GOES CTT observations at the more northern latitudes. The composite width scale of  $\text{CTT} \leq 260$  K increases systematically from south to north (Table 5).

Companion composite traces of CTP (Fig. 22b) show that clouds within the moisture core of the northernmost composite penetrate much deeper into the troposphere (379.6 mb) than clouds within the core of the central and southern composites (475.1 and 579.2 mb, respectively; see also Table 4), and the CTP perturbation and its width scale (see also Table 5) increase with increasing latitude. The connection between both the CTP and CTT characteristics and latitude in the core of the moisture plumes was quite likely driven by physical processes that also impacted the latitudinal dependence of the CLW and RR fields.

TABLE 5. Width scales (km) of SSM/I-observed  $\text{IWV} \geq 2$  cm,  $\text{CLW} \geq 0.2$   $\text{kg m}^{-2}$ , and  $\text{RR} \leq 0.5$   $\text{mm h}^{-1}$ , and GOES-observed  $\text{CTT} \leq 260$  K and  $\text{CTP} \geq 600$  mb as a function of latitude across those composite moisture plumes containing greater than 2 cm of IWV observed by SSM/I.

Latitude bin	IWV $\geq 2$ cm	CLW $\geq 0.2$ $\text{kg m}^{-2}$	RR $\geq 0.5$ $\text{mm h}^{-1}$	CTT $\leq 255$ K	CTP $\leq 600$ mb
<25°N	449.8	114.8	0.0	—	—
25°–30°N	370.7	121.1	30.7	21.1	118.0
30°–35°N	351.3	182.2	159.3	410.3	499.1
35°–40°N	298.0	267.2	252.8	885.6	768.0

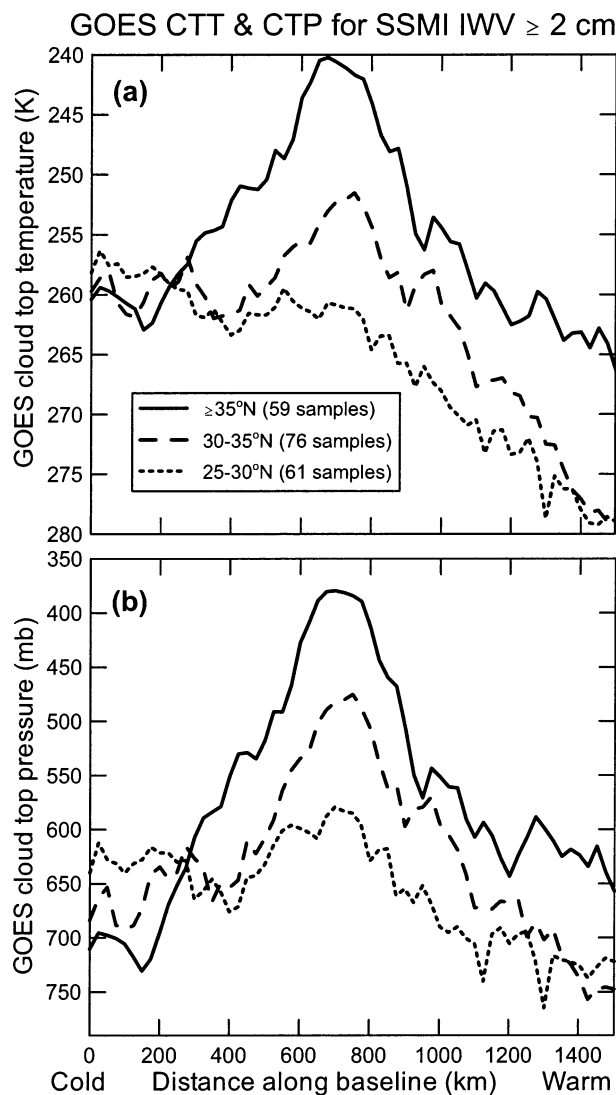


FIG. 22. Composite baselines of GOES-observed (a) CTT (K) and (b) CTP (mb) across all moisture plumes containing  $\geq 2$  cm of SSM/I-observed IWV within four discrete latitude bins (latitudes  $\geq 35^\circ\text{N}$ , solid;  $30^\circ\text{--}35^\circ\text{N}$ , dashed;  $25^\circ\text{--}30^\circ\text{N}$ , dotted;  $< 25^\circ\text{N}$ , no data).

## 5. Conclusions

Observations presented in this paper document the narrow nature of the regions responsible for most of the meridional water vapor flux in the midlatitudes. These concentrated regions of enhanced flux, also known as atmospheric rivers, are typically coupled with polar cold fronts. In addition to observationally documenting several key attributes of atmospheric rivers, this study also confirms the model-based conclusions presented by Zhu and Newell (1998) that four to five rivers (within the earth's circumference at midlatitudes) accomplish  $> 90\%$  of the total instantaneous meridional water vapor transport. The detailed CALJET case study of one river shown here revealed that the horizontal vapor flux was focused at low levels in the region of a moisture-laden

prefrontal LLJ, and that 75% of the total observed flux through a 1000-km cross-front baseline was within a 565-km-wide zone  $\sim 4$  km deep. This zone represented  $1.5 \times 10^8 \text{ kg s}^{-1}$  of meridional flux, the equivalent of roughly 20% of the global average at  $35^\circ\text{N}$ .

To evaluate the representativeness of this single case, a method was developed to objectively identify atmospheric rivers using polar-orbiting (SSM/I) and geostationary (GOES) satellite data from the 1997/98 winter season. Because the case study revealed a close correlation between the horizontal distribution of IWV and horizontal water vapor flux, and because IWV is accurately measured by satellite, IWV was used as a proxy to identify atmospheric rivers. The technique yielded 312 baselines, representing 104 sets of observations through many rivers that each showed a narrow, elongated plume of  $\text{IWV} \geq 2$  cm. Composite traces of SSM/I-observed IWV, CLW, and RR and GOES-observed CTT and CTP were then created and used to quantify the characteristics of satellite-observed rivers for the entire winter season (summarized in Tables 2–5).

The single detailed case was found to be representative of the 312-case composite for  $\text{IWV} \geq 2$  cm in terms of both the IWV amplitude (3.09 cm vs 2.81 cm) and the width of the area where  $\text{IWV} \geq 2$  cm (424 km vs 388 km). The composite maximum SSM/I-observed IWV was only 10% greater than the mean of 2.56 cm found by McMurdie and Katsaros (1991) using earlier versions of SSM/I data in a study of 27 cold-frontal cases in the North Pacific. The SSM/I composites also showed that the mean width scales (defined by the 75% cumulative fraction along a 1500-km composite cross-plume baseline) for CLW and RR were 176 and 141 km, respectively, which are both much narrower than the 417 km for IWV. The much narrower width scales for CLW and RR indicate that vertical circulations responsible for cloud and rain formation occurred on a scale less than half as wide as the physical mechanism(s) responsible for the formation of the IWV plumes. Composite traces of GOES CTT and CTP possessed the coldest and deepest cloud tops in the core of the IWV plumes, and the core cloud tops became substantially colder and deeper when the IWV content within these plumes increased. The anticorrelation between the core moisture content and the cloud-top core values may have arisen partly due to latent heating: as the moisture content within IWV plumes increases, latent heating triggered by forced ascent will be more vigorous, resulting in enhanced upward motion and saturated conditions deeper in the troposphere. Those plumes with greater moisture content may also be indicative of stronger and deeper baroclinic zones and attendant vertical circulations that cause saturated conditions deeper into the troposphere.

A latitudinal dependence of the satellite-derived cross-plume river characteristics was established to ascertain key along-plume attributes. The core IWV content did not vary appreciably with latitude. However,

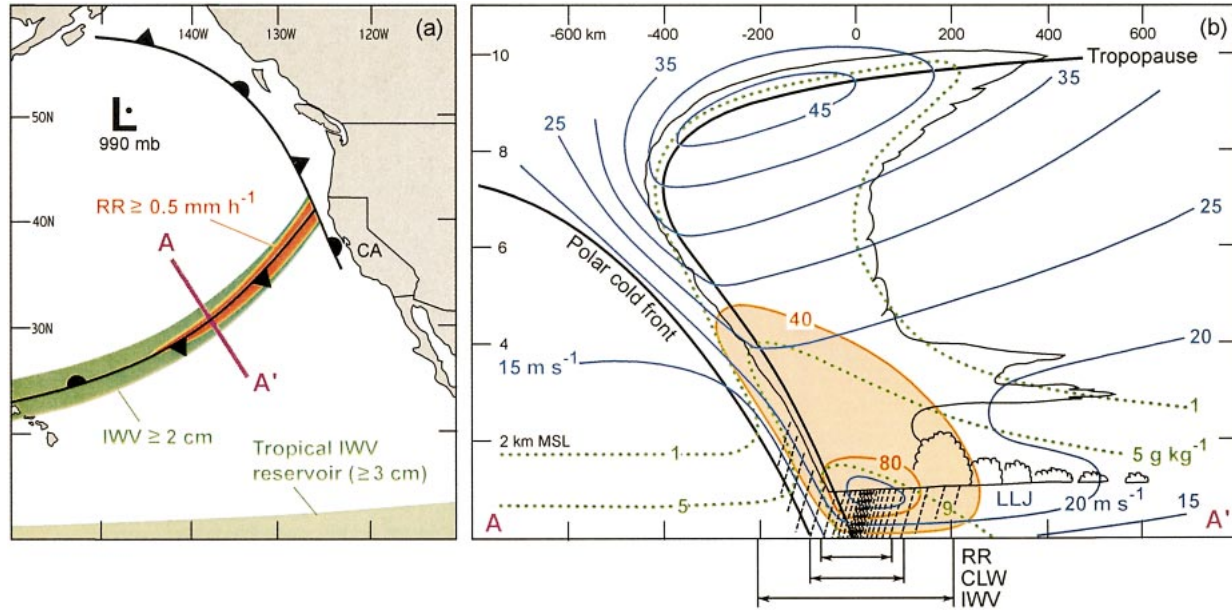


FIG. 23. Conceptual representation of an atmospheric river over the northeastern Pacific Ocean. (a) Plan-view schematic of concentrated IWP ( $IWP \geq 2$  cm; dark green) and associated rain-rate enhancement ( $RR \geq 0.5$  mm  $h^{-1}$ ; red) along a polar cold front. The tropical IWP reservoir ( $>3$  cm; light green) is also shown. The bold line AA' is a cross-section projection for (b). (b) Cross-section schematic through an atmospheric river [along AA' in (a)] highlighting the vertical structure of the alongfront isotachs (blue contours;  $m s^{-1}$ ), water vapor specific humidity (dotted green contours;  $g kg^{-1}$ ), and horizontal alongfront moisture flux (red contours and shading;  $\times 10^5$   $kg s^{-1}$ ). Schematic clouds and precipitation are also shown, as are the locations of the mean width scales of the 75% cumulative fraction of perturbation IWP (widest), CLW, and RR (narrowest) across the 1500-km cross-section baseline (bottom).

the width scale of  $IWP \geq 2$  cm decreased systematically from south to north, thus suggesting cold-frontal confluence may act to contract the lateral scale of the IWP plumes with increasing distance downstream of the southern terminus of the fronts. In contrast, the peak values of CLW and RR in the core region increased by nearly a factor of 2 and an order of magnitude, respectively, from south to north, while their width scales also increased with increasing latitude. The latitudinal variation of CLW and RR reflects the fact that frontal circulations are generally stronger and broader in the mid-latitude storm track than they are in the subtropics. This variation may also reflect Hadley cell subsidence, which can extend northward to  $\sim 30^\circ N$  in the Northern Hemispheric winter mean. It is intriguing to note that the northward decrease of total IWP (factoring in that the area of  $IWP \geq 2$  cm narrows yet the core value stays constant) appears to be offset by the increasing CLW and RR. While this is suggestive of a conservation of water mass in a Lagrangian sense, future efforts focused on a full water budget study are required to demonstrate this.

The case study and composite results are summarized schematically in Fig. 23. In Fig. 23a the mean position of the composite baseline is shown with respect to the composite cold front and atmospheric river. The vertical structure is shown in Fig. 23b, including the key features identified in the case study and in the satellite and synoptic composites at the position of the composite base-

line where  $RR > 0$ . Overall, Fig. 23 highlights the narrow and shallow nature of atmospheric rivers as well as the elevated position of their core near 1 km MSL. Their relationship to upper- and lower-level jets and vertical frontal circulations and their associated convection, are also shown.

An additional goal of the study was to objectively evaluate the capabilities and limitations of current observing systems to detect atmospheric rivers over the eastern Pacific for operational weather prediction and climate monitoring. SSM/I-observed IWP data are reliable in clouds and light to moderate rain, while GOES IWP measurements cannot be obtained in cloudy regions. The GOES IWP data on the edges of cloud bands associated with atmospheric rivers were not correlated with the SSM/I-observed IWP within these bands. In fact, the IWP values outside a 300-km-wide swath centered on the IWP core are nearly uncorrelated with the core values (i.e.,  $r^2 \approx 0.1$ ), which suggests difficulties in using current data assimilation systems applied to GOES IWP data to try to fill the gap. Nonetheless, new ensemble-based data assimilation systems hold promise for using the GOES data outside the rivers to refine the positioning (but not amplitude) of IWP plumes through use of an appropriate flow-dependent model of background error covariances (Evenson 2003). Additionally, Scofield et al. (2000) have developed a promising compositing technique using both SSM/I and GOES IWP data in combination with operational numerical model

analyses. The analysis of SSM/I data also showed that the surface wind speed measurements are not reliable in the core of the rivers because of frequent blockage by rain. While the newer satellite-borne Quick Scatterometer (QuikScat) sensor offers the capability to observe surface wind speed and direction even under moderate rainfall conditions, there remains substantial uncertainty about how to infer wind conditions aloft where the greatest horizontal water vapor fluxes occur. Thus, current satellite systems are unable to adequately monitor atmospheric river fluxes for operational forecasting or climate monitoring, although the best approach may be to blend the strengths of SSM/I and QuikScat polar orbiters with those of GOES.

Because the characteristics of atmospheric rivers are directly tied to the storm track, and thus to short-term climate variability that influences storm tracks, and at the same time are critical in determining precipitation distributions and amounts, they form an opportunity for further study of the connections between short-term climate variability and the occurrence of extreme precipitation and flooding. For climate models, the filamentary nature, or skewness, of this key phenomenon suggests potential problems with aliasing these narrow features into larger scales. Future studies will investigate both the moisture sources of atmospheric rivers (e.g., frontal confluence, upward moisture fluxes from the sea surface, direct tapping of tropical moisture), as well as the depletion processes (e.g., rainout). This water budget work is especially intriguing in terms of the influence of passage over complex coastal terrain. Examination of variations of stable isotopes of rain and water vapor (e.g., Gedzelman et al. 2003) could provide a valuable technique in such a budget study.

*Acknowledgments.* The CALJET field program was made possible by the dedicated participation of individuals from numerous organizations. We are grateful to all of them, particularly the staff of NOAA's Aircraft Operations Center without whom the invaluable NOAA P-3 aircraft data would not have been possible. We are also indebted to Rolf Langland of the Naval Research Laboratory for helping encourage the CALJET team to target this event for data collection with the P-3. We thank Chris Velden of the University of Wisconsin—Madison Cooperative Institute for Meteorological Satellite Studies (CIMSS) for collecting and providing the GOES satellite data, Gary Wade (also of CIMSS) for its processing, and Allen White of NOAA/Cooperative Institute for Research in Environmental Sciences for generating the satellite-based composite figures. Jim Adams provided exceptional drafting services. The collection of data and subsequent study presented here were supported by NOAA Research (as part of NOAA's Rapid Response to the strong El Niño of 1997/98), the Environmental Technology Laboratory, and the U.S. Weather Research Program. We also thank three anon-

ymous reviewers at MWR, and two internal reviewers at NOAA, for their helpful comments.

#### REFERENCES

- Bluestein, H. B., 1993: *Synoptic-Dynamic Meteorology in Midlatitudes*. Vol. 2, *Observations and Theory of Weather Systems*. Oxford University Press, 594 pp.
- Bonner, W. D., 1968: Climatology of the low-level jet. *Mon. Wea. Rev.*, **96**, 833–850.
- Browning, K. A., 1990: Organization of clouds and precipitation in extratropical cyclones. *Extratropical Cyclones: The Erik Palmén Memorial Volume*, C. W. Newton and E. Holopainen, Eds., Amer. Meteor. Soc., 129–153.
- , and C. W. Pardoe, 1973: Structure of low-level jet streams ahead of midlatitude cold fronts. *Quart. J. Roy. Meteor. Soc.*, **99**, 619–638.
- Carlson, T. N., 1991: *Mid-latitude Weather Systems*. Harper-Collins, 507 pp.
- Carter, D. A., K. S. Gage, W. L. Ecklund, W. M. Angevine, P. E. Johnston, A. C. Riddle, J. S. Wilson, and C. R. Williams, 1995: Developments in UHF lower tropospheric wind profiling at NOAA's Aeronomy Laboratory. *Radio Sci.*, **30**, 997–1001.
- Chien, F.-C., C. F. Mass, and P. J. Neiman, 2001: An observational and numerical study of an intense landfalling cold front along the northwest coast of the United States during COAST IOP2. *Mon. Wea. Rev.*, **129**, 934–955.
- Cotton, W. R., and R. A. Anthes, 1989: *Storm and Cloud Dynamics*. Academic Press, 883 pp.
- Ecklund, W. L., D. A. Carter, and B. B. Balsley, 1988: A UHF wind profiler for the boundary layer: Brief description and initial results. *J. Atmos. Oceanic Technol.*, **5**, 432–441.
- Evenson, G., 2003: The ensemble Kalman filter: Theoretical formulation and practical implementation. *Ocean Dyn.*, **53**, 343–367.
- Ferriday, J. G., and S. K. Avery, 1994: Passive microwave remote sensing of rainfall with SSM/I: Algorithm development and implementation. *J. Appl. Meteor.*, **33**, 1587–1596.
- Gedzelman, S., E. Hindman, and X. Zhang, 2003: Probing hurricanes with stable isotopes of rain and water vapor. *Mon. Wea. Rev.*, **131**, 1112–1127.
- Goodberlet, M. A., C. T. Swift, and J. C. Wilkerson, 1990: Ocean surface wind speed measurements of the special sensor microwave/imager (SSM/I). *IEEE Trans. Geosci. Remote Sens.*, **28**, 823–828.
- Heggli, M. F., and R. M. Rauber, 1988: The characteristics and evolution of supercooled water in wintertime storms over the Sierra Nevada: A summary of microwave radiometric measurements taken during the Sierra Cooperative Pilot Project. *J. Appl. Meteor.*, **27**, 989–1015.
- Iskenderian, H., 1995: A 10-year climatology of Northern Hemispheric tropical cloud plumes and their composite flow patterns. *J. Climate*, **8**, 1630–1637.
- Kalnay, E., and Coauthors, 1996: The NCEP/NCAR 40-Year Reanalysis Project. *Bull. Amer. Meteor. Soc.*, **77**, 437–471.
- Keyser, D., and M. A. Shapiro, 1986: A review of the structure and dynamics of upper-level frontal zones. *Mon. Wea. Rev.*, **114**, 452–499.
- Kuhnel, I., 1989: Tropical–extratropical cloudband climatology based on satellite data. *Int. J. Climatol.*, **9**, 441–463.
- Lipton, A. E., 1998: Improved GOES sounder coverage of cloud-broken data fields. *J. Appl. Meteor.*, **37**, 441–446.
- Ma, X. L., T. J. Schmit, and W. L. Smith, 1999: A nonlinear physical retrieval algorithm—Its application to the GOES-8/9 sounder. *J. Appl. Meteor.*, **38**, 501–513.
- McGuirk, J. P., A. H. Thompson, and N. R. Smith, 1987: Moisture bursts over the tropical Pacific Ocean. *Mon. Wea. Rev.*, **115**, 787–798.
- McMurdie, L. A., and K. B. Katsaros, 1991: Satellite-derived inte-

- grated water-vapor distribution in oceanic midlatitude storms: Variation with region and season. *Mon. Wea. Rev.*, **119**, 589–605.
- Mendell, T., 1992: Integration of automated hydrological data. Preprints, *Conf. on Interdisciplinary Approaches in Hydrology and Hydrogeology*, Portland, OR, American Society of Civil Engineers. [Available from NOAA/California–Nevada River Forecast Center, 3310 El Camino Ave., Sacramento, CA 95821-6308.]
- Menzel, W. P., F. C. Holt, T. J. Schmit, R. M. Aune, A. J. Schreiner, G. S. Wade, and D. G. Gray, 1998: Applications of GOES-8/9 soundings to weather forecasting and nowcasting. *Bull. Amer. Meteor. Soc.*, **79**, 2059–2077.
- Namias, J., 1939: The use of isentropic analysis in short term forecasting. *J. Aeronaut. Sci.*, **6**, 295–298.
- Neiman, P. J., F. M. Ralph, A. B. White, D. E. Kingsmill, and P. O. G. Persson, 2002: The statistical relationship between upslope flow and rainfall in California's coastal mountains: Observations during CALJET. *Mon. Wea. Rev.*, **130**, 1468–1492.
- , P. O. G. Persson, F. M. Ralph, D. P. Jorgensen, A. B. White, and D. E. Kingsmill, 2004: Modification of fronts and precipitation by coastal blocking during an intense landfalling winter storm in southern California: Observations during CALJET. *Mon. Wea. Rev.*, **132**, 242–273.
- Newell, R. E., N. E. Newell, Y. Zhu, and C. Scott, 1992: Tropospheric rivers? A pilot study. *Geophys. Res. Lett.*, **19**, 2401–2404.
- Nieman, S. J., W. P. Menzel, C. M. Hayden, D. Gray, S. T. Wanzong, C. S. Velden, and J. Daniels, 1997: Fully automated cloud-drift winds in NESDIS operations. *Bull. Amer. Meteor. Soc.*, **78**, 1121–1133.
- Palmén, E., and C. W. Newton, 1969: *Atmospheric Circulation Systems: Their Structure and Physical Interpretation*. Academic Press, 603 pp.
- Peixoto, J. P., and A. H. Oort, 1992: *Physics of Climate*. American Institute of Physics, 520 pp.
- Ralph, F. M., and Coauthors, 1999: The California Land-falling Jets Experiment (CALJET): Objectives and design of a coastal atmosphere–ocean observing system deployed during a strong El Niño. Preprints, *Third Symp. on Integrated Observing Systems*, Dallas, TX, Amer. Meteor. Soc., 78–81.
- , and Coauthors, 2003: The impact of a prominent rain shadow on flooding in California's Santa Cruz Mountains: A CALJET case study and sensitivity to the ENSO cycle. *J. Hydrometeorol.*, **4**, 1243–1264.
- Rao, P. A., and H. E. Fuelberg, 1998: An evaluation of GOES-8 retrievals. *J. Appl. Meteor.*, **37**, 1577–1587.
- Reynolds, D. W., and A. P. Kuciauskas, 1988: Remote and in situ observations of Sierra Nevada winter mountain clouds: Relationships between mesoscale structure, precipitation, and liquid water. *J. Appl. Meteor.*, **27**, 140–156.
- Schuessel, P., and W. J. Emery, 1990: Atmospheric water vapour over oceans from SSM/I measurements. *Int. J. Remote Sens.*, **11**, 753–766.
- Scofield, R., G. Vicente, and M. Hodges, 2000: The use of water vapor for detecting environments that lead to convectively produced heavy precipitation and flash floods. NOAA Tech. Rep. NESDIS 99, 64 pp. [Available from the National Technical Information Service, 5285 Point Royal Rd, Springfield, VA, 22161.]
- Smirnov, V. V., and G. W. K. Moore, 1999: Spatial and temporal structure of atmospheric water vapor transport in the Mackenzie River basin. *J. Climate*, **12**, 681–696.
- , and G. W. K. Moore, 2001: Short-term and seasonal variability of the atmospheric water vapor transport through the MacKenzie River basin. *J. Hydrometeorol.*, **2**, 441–452.
- Stensrud, D. J., 1996: Importance of low-level jets to climate: A review. *J. Climate*, **9**, 1698–1711.
- Thepenier, R.-M., and D. Cruette, 1981: Formation of cloud bands associated with the American subtropical jet stream and their interaction with midlatitude synoptic disturbances reaching Europe. *Mon. Wea. Rev.*, **109**, 2209–2220.
- Velden, C. S., C. M. Hayden, S. J. Nieman, W. P. Menzel, S. Wanzong, and J. S. Goerss, 1997: Upper-tropospheric winds derived from geostationary satellite water vapor observations. *Bull. Amer. Meteor. Soc.*, **78**, 173–195.
- Weber, B. L., D. B. Wurtz, D. C. Welsh, and R. McPeck, 1993: Quality controls for profiler measurements of winds and RASS temperatures. *J. Atmos. Oceanic Technol.*, **10**, 452–464.
- Weng, F., and N. C. Grody, 1994: Retrieval of cloud liquid water using the Special Sensor Microwave Imager. *J. Geophys. Res.*, **99**, 25 535–25 551.
- Wentz, F. J., 1997: A well-calibrated ocean algorithm for Special Sensor Microwave/Imager. *J. Geophys. Res.*, **102**, 8703–8718.
- White, A. B., D. J. Gottas, E. Strem, F. M. Ralph, and P. J. Neiman, 2002: An automated brightband height detection algorithm for use with Doppler radar vertical spectral moments. *J. Atmos. Oceanic Technol.*, **19**, 687–697.
- , P. J. Neiman, F. M. Ralph, D. E. Kingsmill, and P. O. G. Persson, 2003: Coastal orographic rainfall processes observed by radar during the California Land-falling Jets Experiment. *J. Hydrometeorol.*, **4**, 264–282.
- Whiteman, C. D., X. Bian, and S. Zhong, 1997: Low-level jet climatology from enhanced rawinsonde observations at a site in the southern Great Plains. *J. Appl. Meteor.*, **36**, 1363–1376.
- Zhu, Y., and R. E. Newell, 1994: Atmospheric rivers and bombs. *Geophys. Res. Lett.*, **21**, 1999–2002.
- , and —, 1998: A proposed algorithm for moisture fluxes from atmospheric rivers. *Mon. Wea. Rev.*, **126**, 725–735.
- , —, and W. G. Read, 2000: Factors controlling upper-troposphere water vapor. *J. Climate*, **13**, 836–848.